Vortex dynamics in $NiFe_2O_4$ nanoparticles /CuTl-1223 Superconductor composites

by

Shehzad Ahmed

(209-FBAS/MSPHY/F13)

Supervisor

Dr. Kashif Nadeem

Assistant Professor

Department of Physics

Faculty of Basic and Applied Sciences
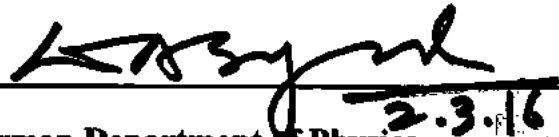
International Islamic University, Islamabad

Vortex dynamics in $NiFe_2O_4$ nanoparticles /CuTl-1223 superconductor composites

by

Shehzad Ahmed

(209-FBAS/MSPHY/F13)

This Thesis submitted to Department of Physics International Islamic University,
Islamabad for the award of degree of MS Physics

Chairman Department of Physics

International Islamic University, Islamabad.
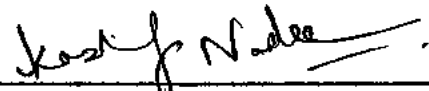
Dean Faculty of Basic and Applied Sciences

International Islamic University, Islamabad.

Final Approval

It is certified that the work presented in this thesis entitled "Vortex dynamics in NiFe$_2$O$_4$ nanoparticles /CuTl-1223 superconductor composites" by Shehzad Ahmed, Registration No. 209-FBAS/MSPHY/F-13 fulfills the requirement for the award of degree of MS Physics from Department of Physics, International Islamic University, Islamabad, Pakistan.

Viva Voce Committee

Chairman _____
(Department of Physics)

Supervisor _____

External Examiner _____

Internal Examiner _____

Forwarding Sheet by Research Supervisor

The thesis entitled "**Vortex dynamics in NiFe₂O₄ nanoparticles /CuTl-1223 superconductor composites**" submitted by **Shehzad Ahmed** (Registration # 209-FBAS/MSPHY/F-13) in partial fulfillment of MS degree in Physics has been completed under my guidance and supervision. I am satisfied with the quality of his research work and allow him to submit this thesis for further process to graduate with Master of Science degree from Department of Physics, as per International Islamic University, Islamabad rules and regulations.

Dr. Kashif Nadeem

Assistant Professor (TTS)

Department of Physics,

International Islamic University,

Islamabad.

Dated: 01-03-2016

IN THE NAME OF ALLAH, THE MOST GRACIOUS, THE MOST MERCIFUL

DEDICATION

To

My Dear Parents

Declaration of Originality

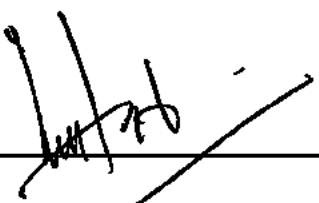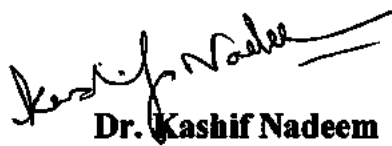I, **Shehzad Ahmed** (Registration No. 209-FBAS/MSPHY/F-13), student of MS Physics (Session 2010-2012), hereby declare that the work presented in the thesis entitled "**Vortex dynamics in NiFe$_2$O$_4$ nanoparticles /CuTl-1223 superconductor composites**" in partial fulfillment of MS degree in Physics from International Islamic University, Islamabad, is my own work and has not been published or submitted as research work or thesis in any form in any other university or institute in Pakistan or aboard.

Shehzad Ahmed

(209-FBAS/MSPHY/F-13)

Dated: _____

Acknowledgement

First and foremost, I would like to say Alhamdulillah, for giving me the strength and health to do this project work until it is done. I would like to express my sincere gratitude to my project supervisor, Dr. Kashif Nadeem, whose encouragement, guidance and support from the initial to the final level enabled me to develop an understanding of the subject, who not only guided me, but kept on challenging me to work even harder. I would also like to thank my senior lab fellows for extending a helping hand at every juncture of need. They really helped me a lot during whole of my project duration.

I am highly indebted to Dr. Jabbar Bhutta and Waqee-Ur-Rehman for guiding me and providing necessary information regarding my project. Last but not the least, I would like to express my gratitude towards my parents and my family, without their support my project had not been completed.

<div align="right">**Shehzad Ahmed**</div>

Abstract

Vortex dynamics in $NiFe_2O_4$ nanoparticles added $(Cu_{0.5}Tl_{0.5})$ $Ba_2Ca_2Cu_3O_{10-\delta}$ (CuTl-1223) superconductor $[(NiFe_2O_4)_x/(CuTl-1223); x = 0, 0.25$ and 0.50 wt. %] have been studied by using magnetic field (0 to 6 T) dependent resistivity versus temperature (ρ-T) measurements. The $NiFe_2O_4$ nanoparticles and bulk CuTl-based superconducting matrix were synthesized separately by sol-gel method and solid-state reaction method, respectively. Initial structural characterization was done by using X-ray diffraction (XRD). XRD analyses confirmed the spinel ferrite structure and tetragonal structure of $NiFe_2O_4$ nanoparticles and bulk CuTl-1223 superconducting matrix, respectively. There were no significant changes were observed in the lattice parameters of bulk CuTl-1223 superconducting matrix with the addition of these nanoparticles. Scanning electron microscopy revealed the granular structure of bulk CuTl-1223 superconductor. The zero resistivity critical temperature ($T_{c\ (0)}$), critical transition temperature onset ($T_{c\ (onset)}$) and glass transition temperature (T_g) were decreased with the increase in applied magnetic field from 0 to 6 T. The normal state resistivity (ρ_{300} (K)) was enhanced with addition of nanoparticle. The double transitions for all concentration of $NiFe_2O_4$ nanoparticles have indicated the existence of vortex-glass phase. The resistive broadening ΔT has been observed with the increase in applied magnetic field. The activation energy (U_o) as determined from the Arrhenius plot of the ρ-T follow a power-law decrease ($U_o \propto H^{-\alpha}$) with magnetic field. The overall decreasing rate in activation energy could be due to diffusion of nanoparticles across the grain-boundaries.

List of Contents

List of Figures

Chapter 1

INTRODUCTION

1.1 Discovery and Evolution of Superconductors

Superconductivity has been known for about a century, the concern in superconducting materials and the mechanism behind such a remarkable phenomenon is still enormous. Superconductivity is one of the most interesting field for research because of its special properties like resistivity, conductivity etc. This phenomenon was first discovered in 1911 by a Dutch physicist Kamerlingh Onnes [1]. He observed it first in mercury which is a low temperature superconductor.
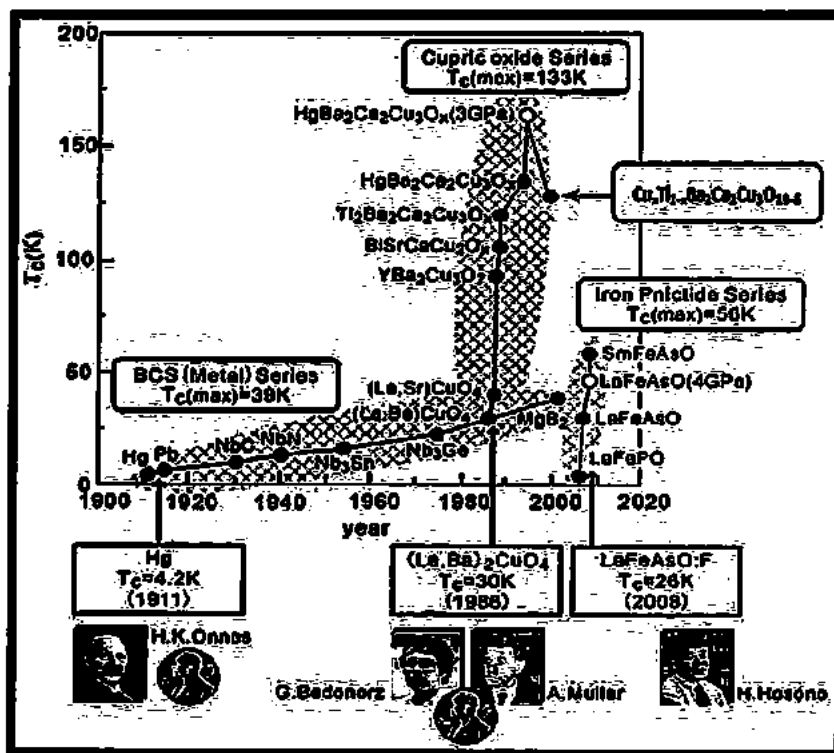
Fig. 1.1: Types of superconductors and advancement in T_c verses years [2].

Superconductors have zero electrical resistance and they can transport current without power losses, so they have a lot of potential applications, for example magnetic suspending trains, magnetic resonance imaging, magnetic levitation devices etc. At low temperatures most of the elements in the periodic table get to be superconducting, while some of them achieve superconductivity at high temperature as shown in Fig. 1.1. The most prestigious property of superconductors is the absence of electrical resistance below critical temperature T_c as shown in Fig. 1.2.
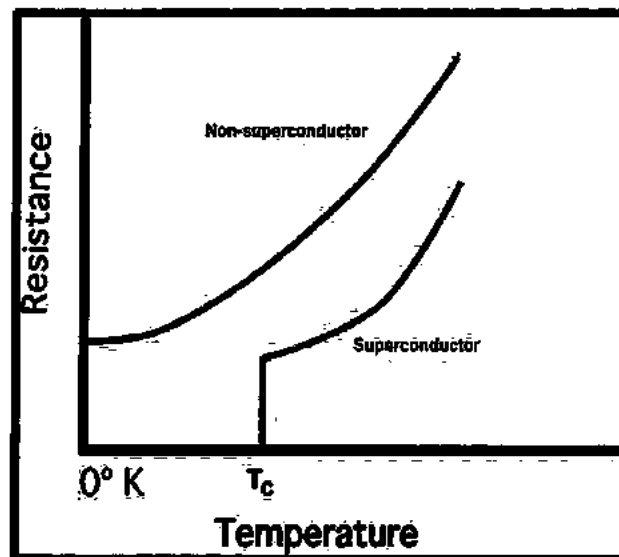
Fig. 1.2 : The phase transition between the normal conductor phase and superconductor phase [3].

Zero resistivity means infinite conductivity. In superconductor, current flows without any resistance because of the pair of electrons named "Cooper pair". But if current density (J_c) becomes smaller than the value of current passes through the conductor, superconductivity vanishes. This phenomenon cannot be described by the conventional Maxwell's equations for electromagnetism, they should rather be modified to incorporate superconductivity. The electromagnetic behavior of a superconductor is not properly defined by the property of zero resistivity. In 1933 W. Meissner and R. Ochsenfeld observed that at temperatures below T_c, the magnetic field was equivalent to zero inside a superconductor and above T_c the superconductor have non-zero field inside it and after it

cooled below T_c [4]. The removal of the magnetic flux in a superconductor, is known as the Meissner effect. A well-known experiment demonstrating the Meissner effect is to put a standard magnet on a superconductor at room temperature and afterward cool it below T_c. Above T_c, the magnetic flux from the magnet penetrates the superconductor but when T_c approaches, all the magnetic flux is forced out of the superconductor as shown in Fig. 1.3, which then lifts the magnet from the superconductor, making it drift above it.
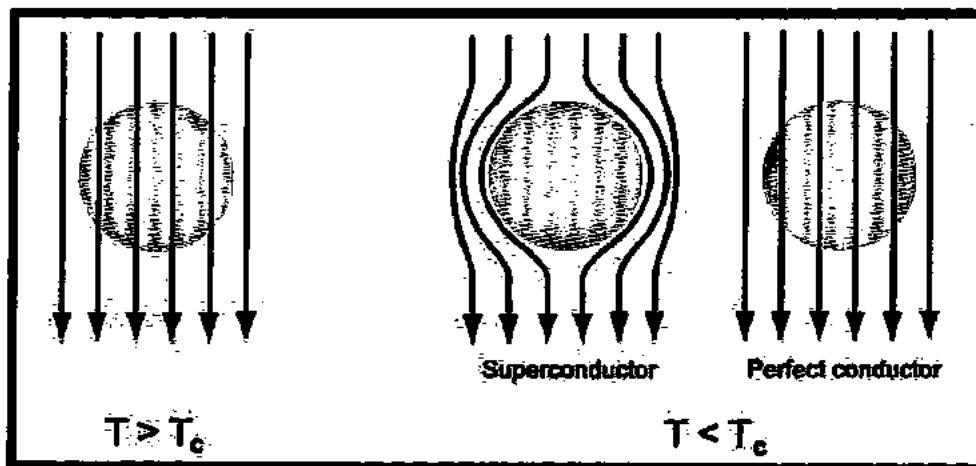
Fig. 1.3: A superconductor expels the magnetic flux in the presence of an external field ($T < T_c$) when cooled below T_c, while the flux would remain the same in a perfect conductor [5].

It had been considered that the field of superconductivity was almost completely understood. However, later on the high-temperature superconductors (HTSCs) have been discovered by Bednoorz and Müller, this field was opened once again [6]. One of the most exciting advancements in this renewed field is the disclosure of new vortex phases, resulting in a rich phase diagram of the vortex matter. Over the years superconductivity has attracted a large attention. In fact several Nobel prizes have been awarded for discoveries within this research area, the most recent in 2003 to A. A. Abrikosov and V. L. Ginzburg for phenomenological theory on HTSCs. In 1987 J. G. Bednorz and K. A. Müller received their Nobel Prize for the discovery cuprates HTSCs. Since then, an impressive amount of work has been done to understand the properties of HTSCs superconductors.

1.2 Critical Parameters of Superconductivity

1.2.1 Critical Temperature (T$_c$)

This is the most prominent temperature at which superconductivity takes place in a superconductor. Below this transition temperature T$_c$, the resistivity of the material is equal to zero as shown in Fig. 1.4 [7].
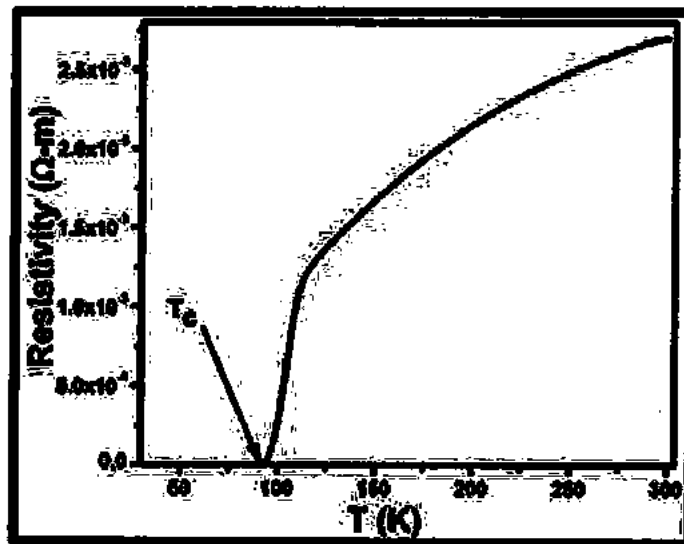
Fig. 1.4: Critical temperature verses resistivity [8].

1.2.2 Critical Magnetic Field (H$_c$)

The superconductivity of the material will be demolished and the normal resistance can be rebuilding up from the diligence of magnetic field. The applied field at which superconductivity vanishes is recognized as "Critical Magnetic Field". This is denoted by H$_c$. Silsbee give the comparison among H$_c$ vs. T as shown in Fig. 1.5 [9, 10].

$$H_c = H_{c0}\left[1 - \left(\frac{T}{T_c}\right)^2\right]$$
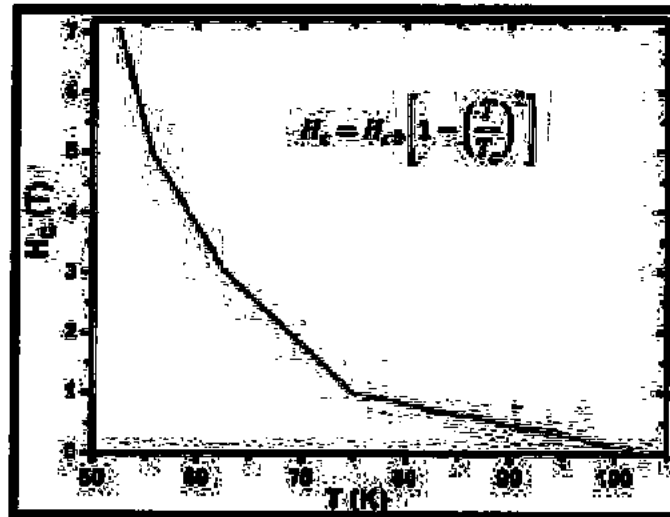
Fig. 1.5: Applied magnetic field verses temperature [9].

1.2.3 Critical Current Density (J_c)

The superconductor loses its superconductivity with the increase in current (I) at certain point. That point is called critical current and is denoted by J_c. It has encouraging applications in the field of wire technology [11].
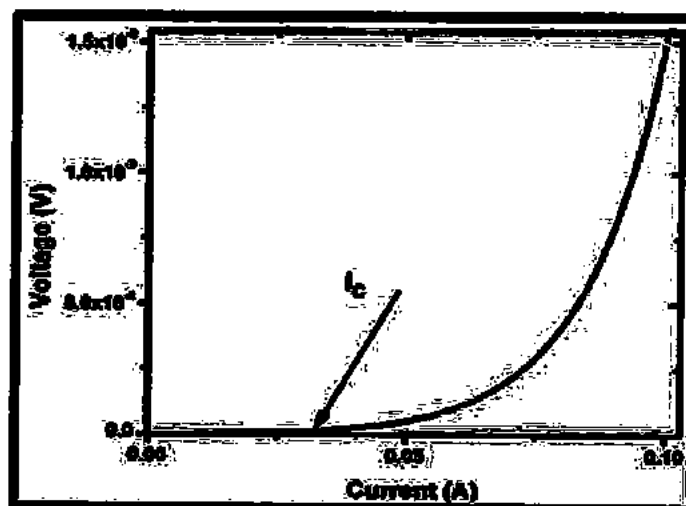
Fig. 1.6: Superconductor I-V curve [11].

1.3 Type-I and Type-II Superconductors

Superconductors discovered first are named as type-I superconductors. They have a simple phase diagram as shown in Fig. 1.7. For type-I superconductors, the material is always in the Meissner effect state and expels magnetic field below $H_c(T)$ e.g. tin, mercury etc. They illustrate perfect diamagnetic behavior due to which they expel magnetic fields. There is only one point in the phase diagram where such statement goes wrong is zero applied magnetic field. The induced applied magnetic field cancels due to rapid change in superconducting state to normal state.
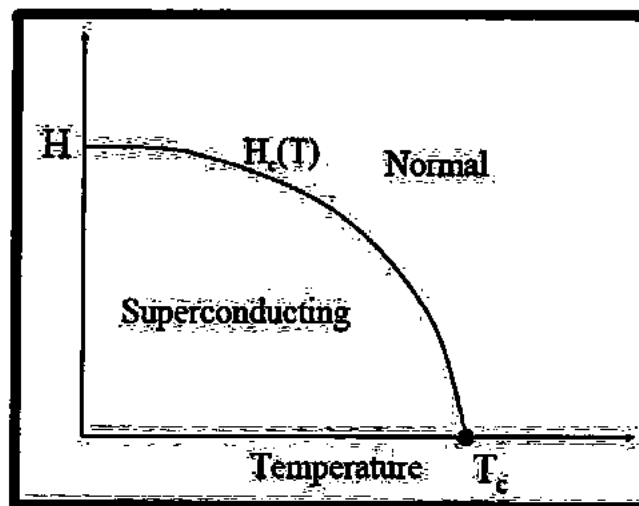
Fig. 1.7: Type-I superconductor phase diagram [12].

In 1930, type-II superconductors were discovered and in 1957 Abrikosov explained it theoretically. Type-II superconductors have a slightly more complex phase diagram as shown in Fig. 1.8. They do not change rapidly from superconducting state to normal state. [13]. They have two thermodynamic critical fields, H_{c1} and H_{c2}. Below H_{c1} type-II superconductors have zero resistivity, they expel magnetic field and their normal state is above H_{c2}. Type-II superconductors are different from type-I because of two critical fields. For $H_{c1} < H < H_{c2}$, magnetic-flux will penetrates into the vortices of superconductor with a quantized quantity of magnetic flux. The electrons inside the cores

of these vortices are in the normal state, whereas the electrons outside the cores are in the superconducting state.
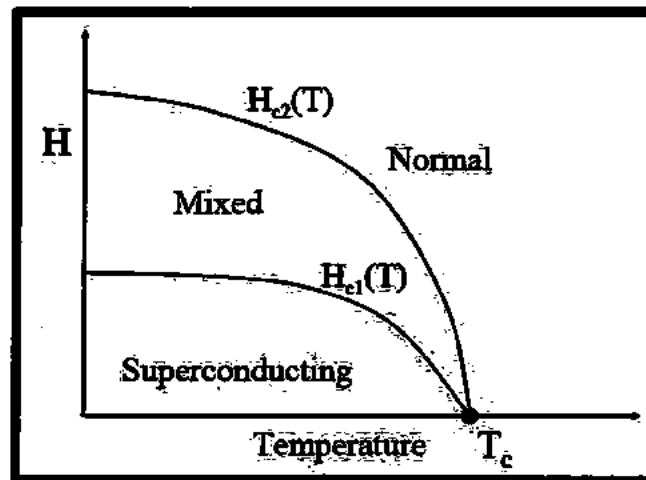
Fig. 1.8: Type II superconductor phase diagram [13].

When vortices come in a superconductor, it is called the vortex state or mixed state. When a current is applied, the vortices move because of the Lorentz force and the electrons in the vortex cores can dissipate energy. Hence there is zero resistance and non-superconducting mixed state.

1.4 Vortex Glass Transition

In 1985, the highest T_c of superconductor was 23 K. In 1986 a new type was discovered with $T_c = 35$ K and soon a new materials with $T_c = 92$ K discovered. These new materials gave rise to re-testing of all faces of superconductivity and are named HTSCs. Fisher, Fisher and Huse (FFH) predicted the beginning of a new phase in superconductors called the vortex-glass phase [14-15]. FFH predicted that dissipation caused in the mixed state of type-II superconductors is due to vortices. At low temperatures the vortices should become pinned thus allowing a passage to a superconducting state is called the vortex glass phase transition as shown in Fig. 1.9.
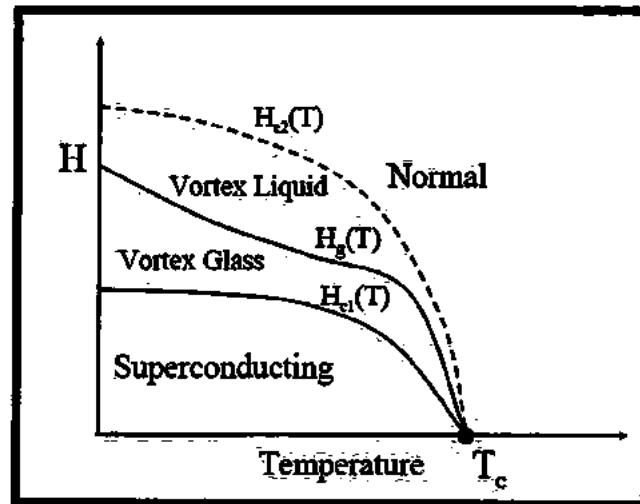
Fig. 1.9: Vortex-glass to liquid phase transition in Type-II superconductors [15].

The increase in temperature will permit the vortices to start their motion and dissipate energy, thus H_{c2} is no more a phase transition but a wide, continuous crossover to the normal state. Thus, the normal-superconducting transition is required as the vortices suspend at $H_g(T)$. Since the vortices are not expelled of the superconductor and there is no energy cost to slow the dynamics of the vortices, the vortex glass phase transition is required to be second-order.

1.5 BCS Theory and Cooper pair

In classical physics the metals have resistance which is due to lattice's vibrations (phonons) and collision of free electrons. The scattering of electrons from the defects or impurities is also responsible for the resistance inside the conductor. The macroscopic theory of superconductivity was discovered in 1957 by J. Bardeen, L. Cooper and J. R. Schrieffer called BCS Theory [16]. The fundamental characteristic of this theory is about two electrons in the superconducting material which are capable to make bound-pairs named Cooper-pairs. This theory appears unreasonable because electrons generally repel each other due to same charges. When electron goes on the lattice and the positive subatomic particles tries to attract it, inducing a deformation from their normal places.
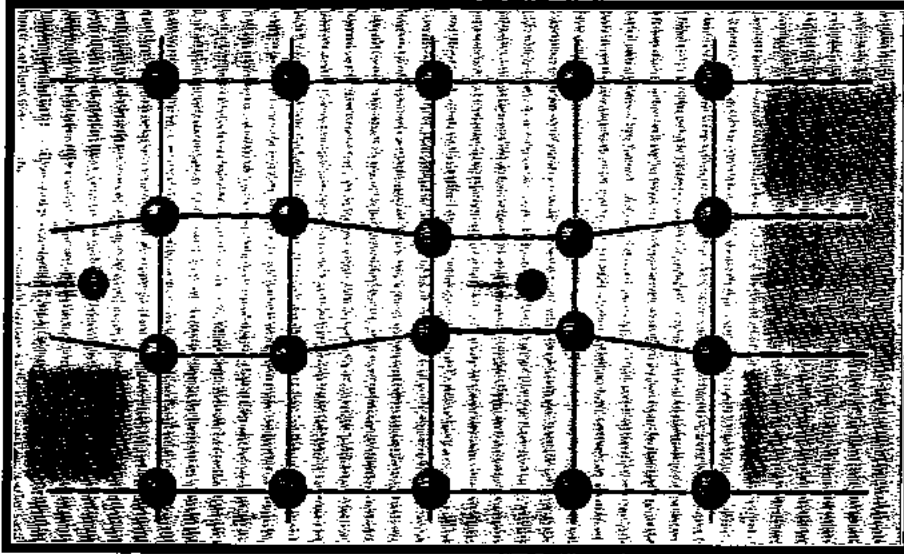
Fig. 1.10: Motion of cooper pairs at extremely low temperatures [16].

The second Cooper pair partner appears and is pulled by the moved subatomic particles, this second electron can simply be pulled to the lattice deformation if they have enough ions to bring back to its equilibrium places. The entire linear momentum of a Cooper pair should be zero. This intends them to move in reverse ways as shown in Fig. 1.10.
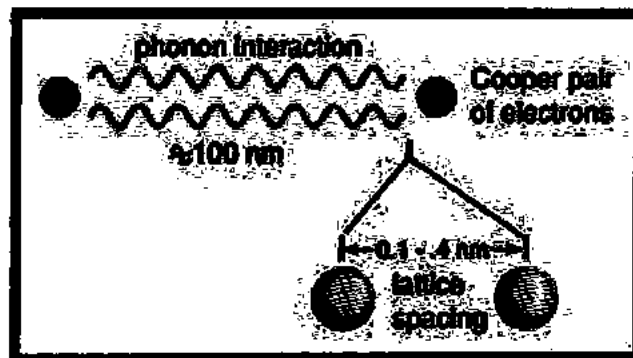
Fig. 1.11: Phonon interaction and lattice spacing between Cooper pairs of electrons [17].

In case of minimal energy site no collisions occurs within the lattice. A small energy is required to demolish the superconducting phase and come through normal which is called the energy-gap as shown in Fig. 1.11 [17].

1.6 Ginsburg Landau (GL) Theory

In 1950, Ginzburg and Landau applied Landau's general theory of phase transitions to superconductors. They introduced a complex superconducting order parameter ψ and expressed the free-energy function in terms of a series expansion of this order parameter and applied fields. This phenomenological theory which does not explain the microscopic origin of superconductivity, because it is mathematically much easier than the microscopic theory. Since the free-energy functional is a series expansion in ψ it is strictly valid only in the vicinity of the superconducting transition, that is $T_c - T < T_c$. Imagine the slimness of $|\psi|$ in terms of its gradient, equation which can represent all the parameters can be showed as

$$F = F_n + \alpha |\psi|^2 + \frac{\beta}{2}|\psi|^4 + \frac{1}{2m}|(-i\hbar\nabla - 2eA)\psi|^2 + \frac{|B|}{2\mu_o} \quad \dots\dots\dots\dots(1.1)$$

Where α and β were handled as parameters, F_n is normal phase Gibbs free energy, e is charge of an electron, m is the effective mass, A is magnetic flux. Vector potential and B is magnetic field. Considering the derivative of the free energy to determine the result we can acquire GL equations as,

$$\alpha |\psi| + \frac{\beta}{2}|\psi|^2 + \frac{1}{2m}(-i\hbar\nabla - 2eA)^2\psi = 0 \quad \dots\dots\dots\dots(1.2)$$

$$j = \frac{2e}{2}\text{Re}\{\psi^*(-i\hbar\nabla - 2eA)\psi\} \quad \dots\dots\dots\dots\dots(1.3)$$

Where J is the current density without any loss and re-expresses the real part, although Eq. 1.3 demonstrating the rate of magnetic field applied [18].

1.7 Coherence length (ξ) and Penetration Depth (λ)

From the GL theory the outcomes were the coherence length (ξ) and penetration depth (λ). It comparison is shown in Fig. 12.

The coherence length,

$$\xi = \sqrt{\frac{\hbar^2}{2m|\alpha|}}$$ ....(1.4)

The penetration depth of the superconducting phase can be written as

$$\lambda = \sqrt{\frac{m}{4\mu_o e^{2\psi^2}}}$$ ....(1.5)

In the absence of applied magnetic field the equilibrium is presented by (ψ_o) which shows that the external applied magnetic field passes to the surface of the superconductor [19]. The ratio among ($K = \frac{\lambda}{\xi}$) represents the GL parameters.

For Type-I superconductors, $0 < K > \frac{1}{\sqrt{2}}$

For Type-II superconductors, $K > \frac{1}{\sqrt{2}}$
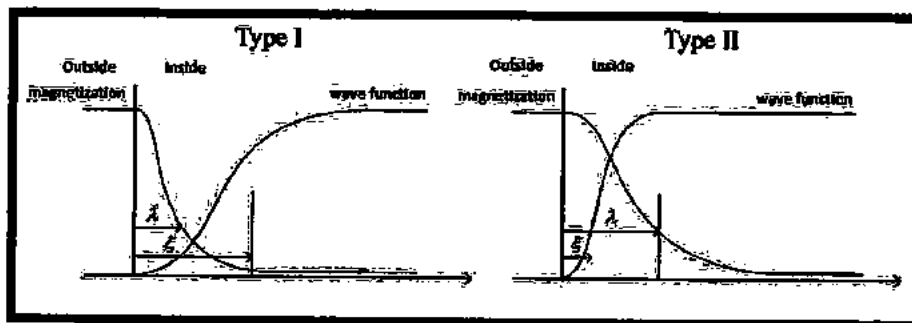
Fig. 1.12: Coherence length and penetration depth comparison for Type-I and Type-II superconductors [20].

1.8 Structure of Cuprate High Temperature Superconductors

The general structure of cuprate HTSCs superconductor single unit cell is shown in Fig. 1.13 [21], which demonstrates the superconducting blocks and the charge blocks in HTSCs. The superconducting blocks generally combined with two charge blocks. This block provides path to conducting electrons as charge block act as charge source. The HTSCs comprise of CuO_2 layers and these layers are located on one another on Ca layers [22]. The excess of CuO_2 layers is responsible for high T_c and this fitting gets significant for high anisotropy in steady conducting and superconducting properties. The conduction is a lot anisotropic parallel to CuO_2 plane. The HTSCs comprise of CuO_2 layers and these layers are located on one another on Ca layers [22]. The excess of CuO_2 layers is responsible for high T_c and this fitting gets significant for high anisotropy in steady conducting and superconducting properties. The conduction is a lot anisotropic parallel to CuO_2 plane. The ceramic compounds are not uniform simply chain of connected grains which disturb the rate of flow of current. Throughout the shaping of the crystal, it is assured that all impurities are gathered at grains limit which block the current. The angle among grains too blocks the flow of super current [23-24].
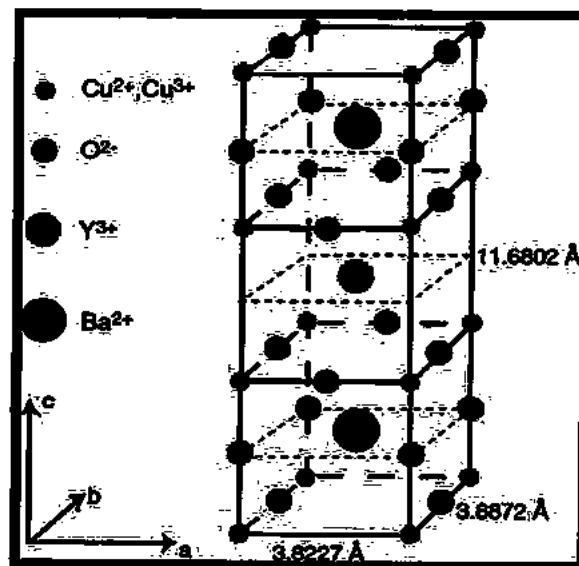
Fig. 1.13: Structure of a single unit cell of HTSC YBCO [21].

1.9 Vortex dynamics

The vortices are not randomly spaced in a clean sample. The vortex dynamics depends on several different forces. One is the Lorentz force, which tries to move the vortices, second is the pinning force which mission is to lock the vortices in normal conducting defects in the superconductor, and third is the elastic energy of the vortex lattice due to vortex-vortex interactions. There are also thermal energies, and at high enough temperatures (high thermal energies) the pinning barriers become very small compared to the thermal energies and that region is called the flux flow region. All these energies together form the phase diagram for high temperature superconductors. At a certain temperature, the vortex lattice melts into a so called vortex liquid, below this temperature there is a so called vortex solid.

The super current circulating every vortex creates a repulsive force keeping them as far as possible from each other, even pushing them out of the superconductor. But above H_{c1} the lowest energy is with vortices, so there is a force trying to maintain a constant flux density in the superconductor and prevent vortices from leaving the sample. The balance between these two forces creates equilibrium where the vortices are held in a triangular lattice. The movement of vortices creates an electric field parallel to the current J, this electric field causes the superconductor to be resistive as shown in Fig. 1.14. From this it can be concluded that there must exist a force, preventing the vortices from moving around otherwise type-II superconductors would not exist.

This force comes from the defects in the material and the phenomenon is known as vortex pinning. Pinning is most effective at low temperatures, when the thermal fluctuations are low, because at higher temperatures the flux lines can move, even though the current density is less than J_c. When the current density is larger than J_c the viscous force is the only force counteracting vortex movement. A measure of this is called the flux flow resistivity.
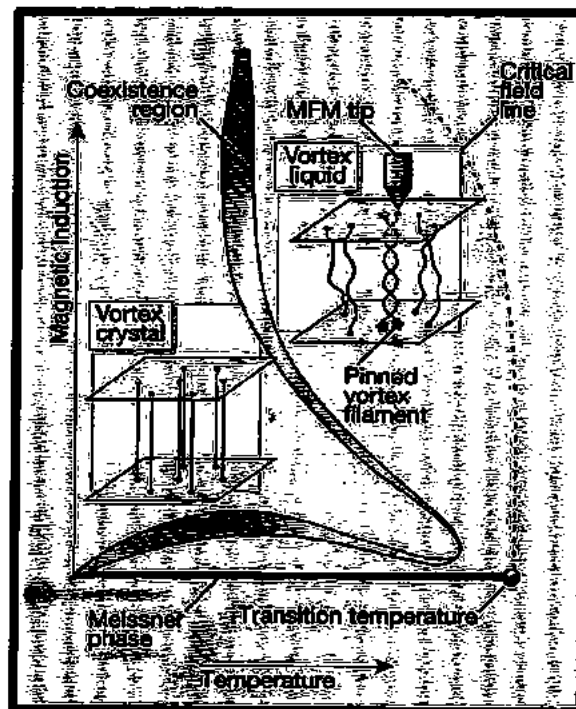
Fig. 1.14: Vortex dynamics in Type-II superconductors [25].

At high temperature, the thermal energy can be high enough to make flux lines to jump from one pinning-center to another. This phenomenon is called flux creep [25-26], and the jump rate is given from activation energy of the pinning barrier. The probability of a jump in one direction is the same as in all directions if there is no current applied. But when a current is applied a flux density gradient is introduced, which favors jumps in the direction given by the Lorentz like force on the vortices [27-28].

1.10 Thermally assisted flux motion

The Type-II superconducting materials show Ohmic behavior at low temperature in magnetic field. In that case the pinning-barriers are very prominent as compared to the thermally energy but still finite. The Thermal Assisted Flux Flow (TAFF) model describes the physics in this state. This model was introduced in 1989, three years after the discovery of HTSCs in 1986 [29]. It is possible to express the resistivity ρ_o and pinning energy U_o are flux and temperature dependent. It is seen that

the logarithm of the resistivity is roughly proportional to the inverse of the temperature. The graph of lnρ as a purpose of 1/T is known as an Arrhenius plot and the linear low resistance part is called the TAFF region [30].

1.11 Nano science and Nanotechnology

"Nano" is the Greek word which means dwarf. Nowadays "Nano" is a prefix which means magnitude 10^{-9} and then nanomaterial are determined as a material having dimension below the range of 100 nm. Big attempts have been made to realize and control these materials. Nanoscience is the area whose research is centered on the study nanoscopic systems of physics, chemistry, biology, etc. as shown in Fig. 1.15 [31]. Nanostructures have unlike properties when comparison with the bulk materials.
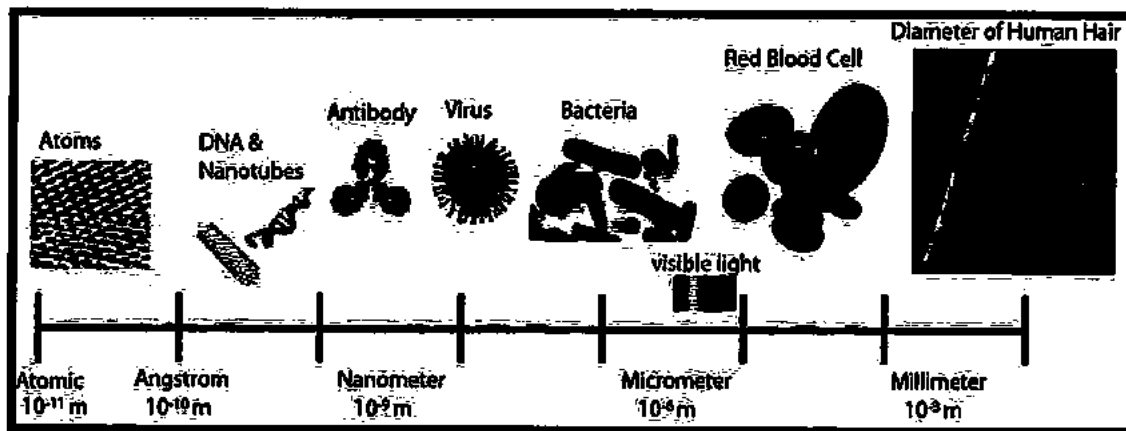
Fig. 1.15: Comparison of the nanoscale [29].

1.12 Surface to Volume Ratio

When size of a material is decreases the ratio among the surface and the volume enhance. The increase of the surface area contributes in an increase of superficial atoms, which are more responsive because their interphase comprising free atomic orbitals [32]. The surface to volume ratio is associated with the surface tension, which is higher for nanoparticles as shown in Fig. 1.16. This

uncomfortable energetic state makes the collection and concretion of the nanostructured materials to reduce the superficial energy.

sides = 3
surface = 3^2 x 6 = 54
volume = 3^3 = 27

surface/volume = ●

sides = 2
surface = 2^2 x 6 = 24
volume = 2^3 = 3

surface/volume = ●

sides = 1
surface = 1^2 x 6 = 6
volume = 1^3 = 1
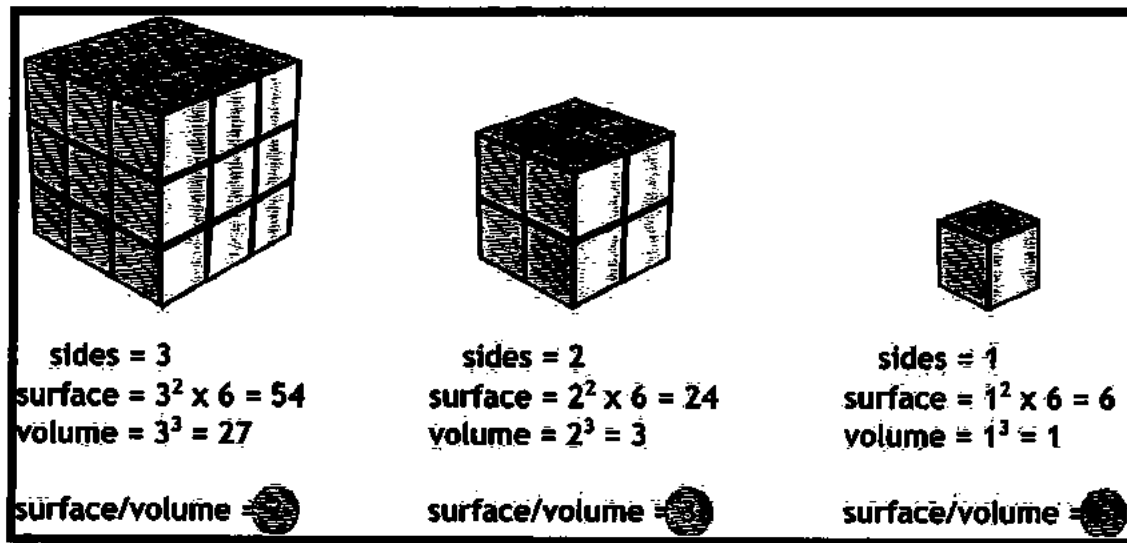
surface/volume = ●

Fig. 1.16: Surface to volume ratios [33].

To avoid collection and keep their nano size, some physico-chemical methods are used to stabilize the nanoparticles [34].

1.13 Ferrite Magnetic Nanoparticles

Ferrite nanostructures are a subclass of magnetic nanoparticles based on an iron oxide structure, the magnetite. Magnetite is an iron and iron oxide (Fe_3O_4), and by substituting the iron by another divalent cation, a new family of compounds is introduced the ferrites (MFe_2O_4). These compounds have been structurally and magnetically studied for ages due to their magnetic applications, and nowadays, new future perspectives to use these compounds in a nanoscale size are being developed [35].

1.14 Spinel Structure

Spinel structure at bulk scale presents a ferri-magnetic behavior, where the orientations of the magnetic spin of the cations situated in the octahedral sites are antiparallel with which ones of the tetrahedral (Td). The spin magnetic moment is in the diagonal direction of the crystallographic cube (direction [1 1 1]). Global net magnetism can be determined by the difference in the contribution of the Oh and Td sites [36]. This modifiable parameter comes from the electronic configuration of each atom, because it gives different magnetic properties depending on their electronic configuration.
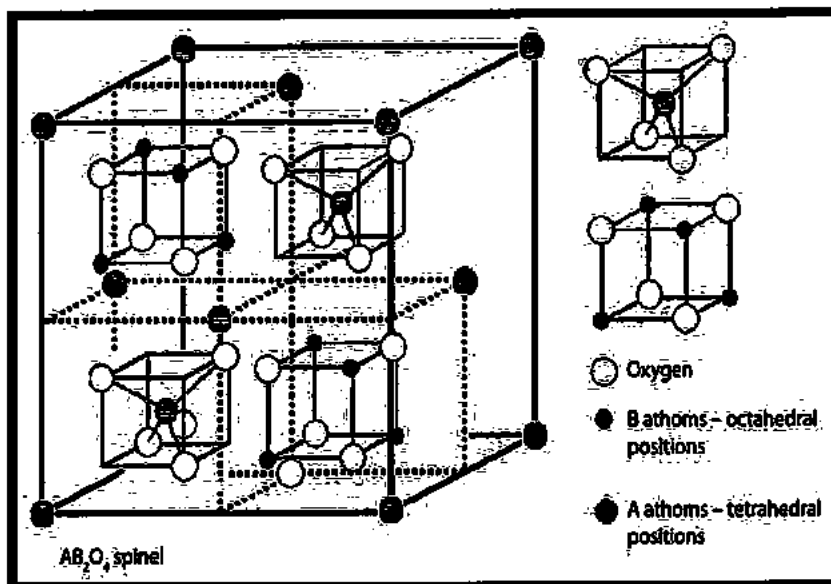
Fig. 1.17: Partial representation of the magnetic unit cell of the spinel structure [38].

Magnetic properties of spinel ferrite have been studied to control, adapt and apply their behavior to new systems in different scientific and technical fields. Nowadays, the development of new nanostructured systems generates a new vision of applications, because ferrites present a super-paramagnetic behavior. Interest in these nanostructured magnets have been increase exponentially last years due to the new generation techniques and applications [37-38].

1.15 Nanoparticles/Superconductor Composites

Different types of nanoparticles were added in different families superconducting matrix. Each type of nanoparticles have different effect on the superconducting properties of the superconductor. One of the promising cuprates HTSCs series, $(Cu_{0.5}Tl_{0.5}Ba_2Ca_{n-1}Cu_nO_{2n+4-\delta})$ (CuTl-12(n-1)n); (n=2, 3, 4,......,) this high T_c cuprates family can be easily synthesized at ambient pressure [39]. $(Cu_{0.5}Tl_{0.5})Ba_2Ca_2Cu_3O_{10-\delta}$ (CuTl-1223) phase have the highest values of almost all superconducting parameters as compared to other phases of this family. So, this CuTl-1223 is one of the most encouraging contender for advance investigation and innovative applications. Its general bulk structure is grainy and porous in nature. Many research groups are working in this field to increase the superconducting properties by reducing these imperfections and enhancing the superconducting volume fraction [40]. The magnetic nanoparticles act as effective pinning centers in the bulk superconductors. The superconducting properties are enhanced by using different oxide nanoparticles and from the addition of In_2O_3 and SnO_2 nanoparticles in bulk CuTl-1223 volume fraction was increased [41-42]. From the addition of Fe_2O_3 nanoparticles the superconducting properties of CuTl-1223 was improved [43]. To continue the series of our project we added magnetic $NiFe_2O_4$ nanoparticles in the bulk CuTl-1223 superconducting matrix and we have found the decrease in $T_{c(0)}$, activation energy and glass transition temperature T_g.

References

1. Kimberlingh Onnes, Comm. Phys. Lab. Univ. Leiden. **122**, 1226 (1911).

2. H. K. Onnes and Akad. Van. Wetensc happen Proc. Royal Acad. Amsterdam **14**, 818 (1911).

3. C. Kittle, Introduction to Solid State Physics, Johan Wiley & Sons (2004).

4. M. Neeraj, Applied Physics for Engineers, PHI Learning Pvt. Ltd. (2011).

5. Harald Ibach, Hans Lüth, Solid State Physics: An Introduction to Principles of Materials Science, 2nd Edition, Springer (1995).

6. J.P. Srivastava, Elements of Solid State Physics, PHI Learning Pvt. Ltd. (2011).

7. Soltan Soltan, Interaction of Superconductivity and Ferromagnetism in YBCO-LCMO Heterostructures, Cuvillier Verlag (2005).

8. F. Ben Azzouz, M. Zouaoui, A. Mellekh, M. Annabi, G. Van Tendeloo, and M. Ben Salem, Physica C, **19**, 455 (2007).

9. Y. Zhao, C. H. Chen, and J. Wang, Supercond. Sci. Technol. **18**, S43 (2005).

10. J. Plain, T. Puig, F. Sandiumenge, X. Obradors, and J. Rabier, Phys. Rev. B **65**, 104526 (2002).

11. S. Y. Chen, and I. G. Chen, Supercond. Sci. Technol. **17**, 7 (2004).

12. N. HariBabu, E. S. Reddy, D. A. Cardwell, A. M. Campbell, C. D. Tarrant, and K. R. Schneider, Appl. Phys. Lett. **83**, 4806 (2003).

13. F. M. Julian, S. Ricart, A. Pomer, L. M. Marzan, J. Nanoscience Tech. **11**, 3245- 3255 (2011).

14. H. Li, M. Ionescu, H. K. Liu, T. Silver, X. L. Wang, and S. X. Dou, IEEE Trans. Appl. Supercond. **15**, 2 (2005).

15. V. Bartunek, and O. Smrckova, J. Supercond. Nov. Magn. **24**, 1241 (2011).

16. E. Zeldov, D. Majer, M. Konczykowski, V. B. Geshkenbein, V. M. Vinokur, and H. Shtrikman, Nature **375**, 373 (1995).

17. X. S. Ling, S. R. Park, B. A. McClain, S. M. Choi, D. C. Dender, and J. W. Lynn, Phys. Rev. Lett. **86**, 712 (2001).

18. Sven Larsson, Chemical Physics: Electrons and Excitations, CRC Press (2012).

19. K. Nakashima, N. Chikumoto, A. Ibi, S. Miyata, Y. Yamada, T. Kubo, A. Suzuki, T. Terai, Physica C **463**, 665 (2007).

20. Hamrita, F. Ben Azzouz, W. Dachraoui, and M. Ben Salem, J. Supercond. Nov. Magn. **26**, 879 (2013).

21. S. Patnaik, A. Gurevich, S. D Bu, S. D. Kaushik, J. Choi, C. B. Eom, and D. C. Larbalestier, Phys. Rev. B **70**, 064503 (2004).

22. S. Dadras, Y. Liu, Y. S. Chai, V. Daadmehr, and K. H. Kim, Physica C **469**, 55 (2009). M. Farbod, and R. M. Batvandi, Physica C **471**, 112(2011).

23. J. Gutiérrez, A. Llordés, J. Gazquez, M. Gibert, N. Romá, S. Ricart, A. Pomar, F. Sandiumenge, N. Mestres, T. Puig, and X. Obradors, Nat. Mater. **6**, 367 (2007).

24. T. G. Holesinger, L. Civale, B. Maiorov, D. M. Feldmann, J. Y. Coulter, J. Miller, V. A. Maroni, Z. J. Chen, D. C. Larbalestier, R. Feenstra, X. P. Li, M. B. Huang, T. Kodenkandath, W. Zhang, M. W. Rupich, and A. P. Malozemoff, Adv. Mater. **20**, 391 (2008).

25. S. Engel, T. Thersleff, R. Huhne, L. Schultz, and B. Holzapfel, Appl. Phys. Lett. **90**, 102505 (2007).

26. T. Puig, J. Gutierrez, A. Pomar, A. Llordes, J. Gazquez, S. Ricart, F. Sandiumenge, and X. Obradors, Supercond. Sci. Technol. **21**, 034008 (2008).

27. P. W. Anderson and Y. B. Kim, Rev. Mod. Phys. **36**, 39 (1964).

28. M. Feigel'man, V. Geshkenbein, A. Larkin, and V. Vinokur, , Phys. Rev. Lett. **63**, 2303 (1989).

29. T. Nattermann, 'Scaling approach to pinning: Charge-density waves and giant flux creep in superconductors'. Phys. Rev. Lett. **64**, 2454 (1990).

30. D. Ephron, A. Yazdani, A. Kapitulnik, and M. R. Beasley, Phys. Rev. Lett. **76**, 1529 (1996).

31. Project on Emerging Nanotechnologies, Woodrow Wilson international center for scholars (www.nanotechproject.org).

32. G. A. Ozin, A.C.Arsenault, L.Cadem rtiri "Nanochemistry; A chemical Approach to nanomaterials" 2nd, RSC publishing, (2009).

33. Guozhong Cao, University of Washington, USA, Nanostructures & Nanomaterials, synthesis, properties & applications, Imperial College Press, UK. (2004).

34. http://www.vacuumschmelze.com/uploads/pics/po2_rapid_cristalin_457_01.gif.

35. R.S. Tebble, D.J. Craik, Magnetic Materials, John Wiley and Sons, New York, (1969).

36. http://www.aic-shanghai.com.

37. Y. Yamamoto, J. Makino, J. Magn. Magn. Mater. **133**, 500 (1994).

38. http://maser.zip.net/images/spinel.gif

39. H. Ihara, K. Tokiwa, K. Tanaka, T. Tsukamoto, T.Watanabe, H. Yamamoto, A. Iyo,M. Tokumoto, M. Umeda, Physica C **97** 282–287 (1997).

40. M.H. Pu, W.H. Song, B. Zhao, X.C. Wu, T. Hu, Y.P. Sun, J.J. Du., Supercond. Sci.Tech. **14** 305–310 (2001).

41. Y.C. Guo, Y. Tanaka, T. Kuroda, S.X. Dou, Z.Q. Yang, Physica C **311**, 65(1999).

42. N. H. Mohammed, A.I.Abou-Aly, I. H. Ibrahim, R. Awad, M. Rekaby, J. Alloy. Compd. **486**, 733(2009).

43. N. H. Mohammad, A. I. Abou-Aly, R. Awad, I. H. Ibrahim, M. Roumie, M. Rekaby, J. Low Temp. Phys. **172** 234(2013).

Chapter no. 2

Literature Review

Mohammad *et al.* [1] studied the CuTl-1223 superconductor's transport properties with the addition of nanoparticles of SnO_2. They use ceramic method for the synthesis of CuTl-1223 superconducting matrix. After the increase in nanoparticles concentration, the samples are analyzed by some different techniques. To study the crystal structures and phase changes XRD is used. EDS analysis is used to examine the absence of nanoparticles of SnO_2 in phase structure. They observed that with the increase of nanosized SnO_2 bettered the stiffness at micro level.

Elokret *et al.* [2] examined the nanoparticles of zinc oxide, synthesized by using co-precipitation technique, they determined that the increase of these ZnO nanoparticles in CuTl-1223 superconductor was inserted because the betterment in the attributes of superconductor with the increase in concentration of ZnO nanoparticles. Enhancement in resistance at grain boundaries and superconductors secondary phase is increased with the increase in nanoparticles concentration. While the decrease in resistance of the grain boundaries and increase in secondary phase was noticed with the addition in ZnO nanoparticles concentration.

Nadeem *et al.* [3] studied the (Ni/NiO)/CuTl-1223 nanoparticles/superconductor composites. They use ceramic method for the synthesis of superconductor and sol-gel method for the synthesis of nanoparticles. Throughout their analysis they determined that the critical temperature (T_c) of the superconducting composite matrix was decreased by increasing Ni/NiO nanostructures, which is due to pinning of mobile free carriers and cooper-pair breaking.

Ghorbani *et al.* [4] studied the vortex-liquid to vortex-glass transition in $Ba_{0.72}K_{0.28}Fe_2As_2$, $Ba_{0.9}Co_{0.1}Fe_2As_2$, and $Ba(Fe_{0.45}Ni_{0.05})_2As_2$ single crystals with T_c = 31.7, 17.3, and 18 K, respectively, by magneto resistance measures. They observed that by doping K results in a high glass

transition boundary near H_{c2}, when magnetic Ni and Co doping cause a low glass line which is far away from the H_{c2}. Their results suggest that magnetization free caused disorder is more prosperous for enhancement of pinning force equated to magnetized caused disorder. Their results show that pinning is responsible for the deviation in the glass states.

Sharma et al. [5] analyzed the temperature dependency on resistivity under applied field of $Bi_2Sr_2CaCu_2O_{8+\delta}$ samples synthesized by sol-gel method. They noticed that $T_{c(0)}$ of the representative composites samples is enhanced from 32-82 K by raising sintering temperature. The increases resistive transition broadening was observed when the sintering temperature was reduced, since $T_{c(onset)}$ is not changed much. They observed superconducting transition under applied magnetic field under T_c was talked about on the basis of TAFF model. The TAFF activation energy U_o has been estimated by using the Arrhenius plots under applied magnetic field. They conceive that the forming temperature and the function of grains are the key factors to be treated for copper based superconductors.

Waqee-ur-Rehman et al. [6] studied the infield response of Al_2O_3 nanoparticles on the bulk CuTl-1223 superconductor. They analyzed that the increase of Al_2O_3 nanoparticles concentration in the CuTl-1223 superconductor will not affect the crystal structure, which shows the presence of nanostructures on the grain-boundaries. The dc-resistivity was noticed with externally field from 0-7 T. The behavior of dc-resistivity and activation energy U_o was expressed by TAFF model. They observed that with the increase in Al_2O_3 nanoparticles concentration activation energy have been decreased due to reduction in flux pinning strength.

Waqee-ur-Rehman et al. [7] synthesized the nanoparticles/superconductor composites samples with different concentration of $CoFe_2O_4$ nanoparticles. They synthesized nanoparticles by using sol-gel method and bulk superconductor by using solid-state reaction technique. According to the infield measurements of the composites samples $T_{c(0)}$ have been decreased to the lower value with the increase in external field. With the Increase in $CoFe_2O_4$ nanoparticles concentration the fluxoid motion have been reduced in the CuTl-1223 superconducting matrix. Activation energy U_o

was estimated from Arrhenius plots, the enhance in the activation energy U_0 have been noticed with the increase in $CoFe_2O_4$ nanoparticles concentration up-to $x = 1.5$ wt. % in bulk CuTl-1223 superconductor.

Sun et al. [8] synthesized the Iron-based superconductor $NdFeAsO_{0.88}F_{0.12}$ by two steps solid-state reaction method and temperature dependent resistivity was evaluated at different fields 0-9 T. Arrhenius plot expresses the tail effect which consists of two resistivity drop phases, normal superconducting transition the weak-links among the grains. The resistivity drops due to weak-link behavior which is based on the Josephson junctions made by the impurity in the grains. These junctions can be cracked by the applied fields, contributing to the unnatural resistivity tails in polycrystalline Iron-based superconducting matrix.

Vinod et al. [9] investigated the infield response of doped $Ba(Fe,Co)_2As_2$ single crystals. Activation energy U_0 can be found out by applying the TAFF model for H||ab and H||c planes. They noticed the power law dependency of U_0 versus H for H||ab and H||c planes, single flux pinning was observed below 7 T for H||ab and for field above 7 T collective pinning was observed for H||c. They also compared some U_0 for the $Ba(Fe,Co)_2As_2$ systems with another superconductors is introduced.

Lu Jun-Chao et al. [10] studied the vortex phase transition in $BaNi_{0.1}Fe_{1.9}As_2$ single crystal having $T_c = 19.40$ K by using magneto-resistance measures. They evaluated resistivity curve under applied fields range 0-13 T for H||c and H⊥c. They determined the efficient pinning potential U_0 from the varied vortex-glass theory model by applying the exponent s. They have also determined the phase diagrams of vortex glass transition temperature T_g for H||c and H⊥c, vortex-crossing over temperature T and the upper-critical field H_{c2}.

Shahbazi et al. [11] investigated the critical current density J_c, flux pinning and magneto resistance analysis of $BaFe_{2-x}Ni_xAs_2$ single crystal under fields 0-13 T and a temperature from 2-20 K. The magneto resistance behavior below T_c expresses Arrhenius behavior, where U_0 is the activation energy. $BaFe_{2-x}Ni_xAs_2$ shows high activation energy with a real imperfect field addiction.

They observed high J_c at zero field and low for 1 T. They also observed flux jumping in magnetic induction loops at low temperature for prominent samples for high J_c in the single crystal.

Eltsev *et al.* [12] studied the vortex liquid phase transition for Pb-doped Bi-2223 single crystal by utilizing the field and temperature of resistivity from 0-6 T. They observed the decrease in temperature near onset resistivity which expresses the power law dependency on temperature indicating approach to vortex-glass transition. They also introduce the magnetic phase plot to define the part of non-zero critical current towards Pb-doped Bi-2223 single crystal.

Mumtaz *et al.* [13] analyzed the superconducting properties of carbon-nanotubes added CuTl-1223 superconductor composites samples. They observed $T_{c(0)}$, $T_{c(onset)}$ and T_g have been decreased with the increase in carbon-nanotubes (CNTs) concentration in the host CuTl-1223 superconducting matrix. They also observed the double transitions for all the composites samples which indicates the presence of vortex-glass phase, the decrease in field dependence of U_0 was observed representing TAFF model and the resistive extending has been noticed with the increase in applied field.

Vinu *et al.* [14] analyzed the dependency of resistive transition on temperature and field of $Bi_{1.6}Pb_{0.5}Sr_{2-x}Eu_xCa_{1.1}Cu_{2.1}O_{8+\delta}$ superconducting matrix. They observed glassy conduct of resistivity for high temperature and fields for Eu/doped specimens as compare to Eu/free specimens, the T_g, $U_0(B)$ and $U_0(T)$ have been increased with the increase in dopant concentration which indicates the efficient pinning of flux lines. This grading is very useful to understand the motion of vortices in HTSCs.

Andersson *et al.* [15] proposed the model for the detailed analysis for vortex liquid state transition, resistivity near a vortex liquid to glass transition-phase. They have found the elaborated numerical understanding among the model discussed and resistivity measurements about disordered, partially-doped $YBa_2Cu_3O_{7-\delta}$ single crystal. Physically interpretations of the example and its relation with other examples of vortex-liquid resistivity transition are also studied.

Ansari et al. [16] analyzed the dependency of temperature on resistivity of nano-diamond doped MgB_2 superconducting matrix under applied fields 0-8 T. They observed that Irreversibility was increased from the doping of nano-diamond. They find out the activation energy of TAFF region from Arrhenius law. The field dependency of energy of activation of diamond nanostructures doped in MgB_2 superconducting matrix was estimated from slope of running component of the Arrhenius-plots and which shows rapid decreased with the increase in field. Hence, the current density of this specimen will be increased for applied applications.

Naqib et al. [17] studied the quality of resistive transition for crystalline $YBa_2Cu_3O_{7-d}$ superconducting thin-films under different fields along the c-direction throughout a broad rate of doped-holes in the CuO_2 planes. The temperature and field dependency of resistivity have been studied from TAFF model, the flux flow activation energy U_0 has been evaluated from the analysis of this model. The low-transition area of the resistivity data can be discussed from the activation energy and H changes quickly due to which resistivity is changes. U_0 is related to the pinning potential and superconductors condensing energy. They also observed that normal phase pseudo-gap immediately involves superconductors condensing energy, a clear balance between H_0 and the P-Gap energy scale was determined.

Dadras et al. [18] analyzed the response of CNTs on structure and superconductor transport attributes of $YBa_{2.0}Cu_{3.0}O_{7-\delta}$ composites specimens. This was synthesis by ceramic method. XRD examination sustains the orthorhombic crystallization structure of the samples. No significant change was observed in $T_{c(0)}$ with the increase in nanoparticles concentration and increasing the field. The SEM images demonstrate the CNTs formation between the grains. Their observances propose that the increase of CNTs to the Y-123 superconducting matrix improves the electrical association among the grains of the superconductor to increase the J_c.

Vinu et al. [19] studied that the vortex liquid resistive transition is about the vortex glass state in Ho doped Bi and Pb-2212 superconducting composite. A prominent extending in transition was observed under applied field, which is the evidence of the thermal variation in the vortex matter,

therefore the altered vortex glass to liquid transition hypothesis was used to estimate the activation energy. They also demonstrate the vortex-glass behavior of dc-resistivity at high temperature. Their outcomes also indicates the enhancement in T_g and U_o which expresses that flux lines are efficaciously trapped and in the vortices are in glass state.

Bhoi *et al.* [20] evaluated the temperature and field dependency on resistivity of the polycrystalline $PrFeAsO_{0.60}F_{0.12}$ samples in normal and superconducting states. The superconductor transition $T_{c(onset)}$ decrease with the increase in applied field 0-14 T. Upper critical field $H_{c2(0)}$ is calculated by utilizing the GL theory and the WHH equation above 100 T. They estimated the resistivity under $T_{c(0)}$ which shows Arrhenius act due to TAFF of vortices. The activation energy U_o is specified from the Arrhenius plot of the resistivity which exhibits a power-law dependence on applied field.

References

1. N. H. Mohammad, A. I. Abou-Aly, I. H. Ibrahim, R. Awad, and M. Rekaby, J. Alloys and Compd. **486**, 733 (2009).

2. M. M. Elokret, R. Awad, A.A. El-Ghany, A.A.Shama, and A. El-wanis, J.Supercond. Nov. Magn. **24** 1345, (2011).

3. K. Nadeem, F. Naeem, M.Mumtaz, S. Naeem, A.Jabbar, I. Qasim and Nawazish A.Khan, Ceramics Int. **40**, 13819–13825 (2014).

4. S. R. Ghorbani, X. L. Wan, M. Shabazi, S. X. Dou, K. Y. Choi , Phys. Rev. B, **431**, 67–80, (2014).

5. Devina Sharma, RanjanKumar, V.P.S.Awana, S. S. Commun. **152**, 941–946, (2012).

6. M. Waqee-ur-Rehman, Irfan Qasim, M. Mumtaz, Phys. Rev. B, **476**, 37–40, (2015).

7. M. Waqee-ur-Rehman , Irfan Qasim , M. Mumtaz , K. Nadeem , S. Qamar, J. Alloys and Compd, **657**, 348-352 (2016).

8. Y. Sun, Y. Ding, J. C. Zhuang, L. J. Cui, X. P. Yuan, Chin. Phys. B **13**, 239-205, (2011).

9. Vinod, Shilpam Sharma, A. T. Satya, C. S. Sundar and A. Bharathi Phys. Rev. E, **178**, 334, (2012).

10. Lu Jun-Chao, Yu Yi, Pi Li, Chin. Phys. B **23**, 397-405, (2014).

11. Mahboobeh Shahbazi , Xiaolin Wang, Z W. Lin , Adv. Materials, **1**, 107148 (2013).

12. Yu. Eltsev, S. Lee, K. Nakao, S. Tajima, Phys. Rev. C, **480**, 269–282, (2010).

13. M. Mumtaz, Ghulam Hussain, M. W. Rabbani, M. Waqee-ur-Rehman, Irfan Qasim, AIP Advances **5**, 107148 (2015).

14. Surendran Vinu, Pallian Murikoli Sarun, Razia Shabna, Solid State Sciences **11** 1530–1534, (2009).

15. M. Andersson, A. Rydh, Phys. Rev B, **63**, 184511 (2012).

16. Intikhab, A. Ansari , M. Shahabuddin , Nasser Saleh Alzayed , Arpita Vajpayee, V .P. S. Awana , H. Kishan, Phys. Rev. C, **470**, 369–372, (2010).

17. S. H. Naqib, R. S. Islam, Phys. B, **24**, 017402, (2015).

18. S. Dadras , Y. Liu , Y.S. Chai , V. Daadmehr , K.H. Kim, Phys. Rev. C, **469**, 55–59, (2009).

19. S. Vinu, P. M. Sarun, R. Shabna, A. Biju, and U. Syamaprasad J. A. Phys. **105**, 123901 (2009).

20. D Bhoi, L S Sharath Chandra, P Choudhury, V Ganesan and P Mandal "The magnetoresistance of a PrFeAsO1−xFy superconductor" Supercond. Sci. Technol. **22** (2009).

21. M. Shahbazi, X. L. Wang, S. R. Ghorbani, M. Ionescu, O. V. Shcherbakova, F. S. Wells, A. V. Pan, S. X. Dou, K. Y, J. A. Phys. **26**, 445, (2013).

Chapter no. 3

Synthesis and Experimental Techniques

For the synthesis of high temperature superconductors numerous techniques have been introduced. These techniques are employed to prepare fine crystalline structures, consuming synthetic or actually existing crude materials.

3.1 Solid-State Reaction Technique

Ceramic method or solid-state reaction method is very frequently used method for the preparation of polycrystalline materials or oxide materials. The choice of reactants relay upon the conditions and nature of reaction and products respectively. As the surface area increases the rate of reaction so, the refined material is used for the preparation of crystalline structures. Calculated amount solid reactants are then mixed by using mortar and pestle. To make the mixture homogeneous organic liquids are added which will be then evaporated during process of mixing. The mixture after evaporation must be pelletized in order to increase the contact strength among grains. After pelletlization the mixture is then placed in vessels made up of quartz for heat treatment. The technique, Solid state reaction play vital role for preparing numerous cuprates. To get ceramic materials with various solid material metal oxides, nitrates, carbonates and salts all are mixed and then the mixture experience heat treatment till reaction completion [1]. Tl_2O_3 is one of the highly toxic materials [2] that's why caution safety must be pronounced in the preparation of thallcuprates. While the Tl-based superconductors with high T_c were studied by two scientists Sheng and Hermann [3-4] by firing up precursor (Ba-Ca-Cu-O) with (Tl_2O_3) powder for atleast 3 to 5 min at temperature of ~ 880–910 °C following oxygen supply. In case of higher unpredictability of Tl-components, the synthesis of the pure phase samples goes difficult. In order to prevent loss of Thallium from the samples, it should be wrapped in silver or gold foils because they don't react with the material.

3.2 Nanoparticles synthesis

3.2.1 Top-down Approach

Top-down approach is also known as physical method. By using this method nanoparticles are produced by reducing the size, subtracting or sub-division of the bulk materials. Some of the most commonly used physical methods are ball milling, arch discharge and thermal methods [5].
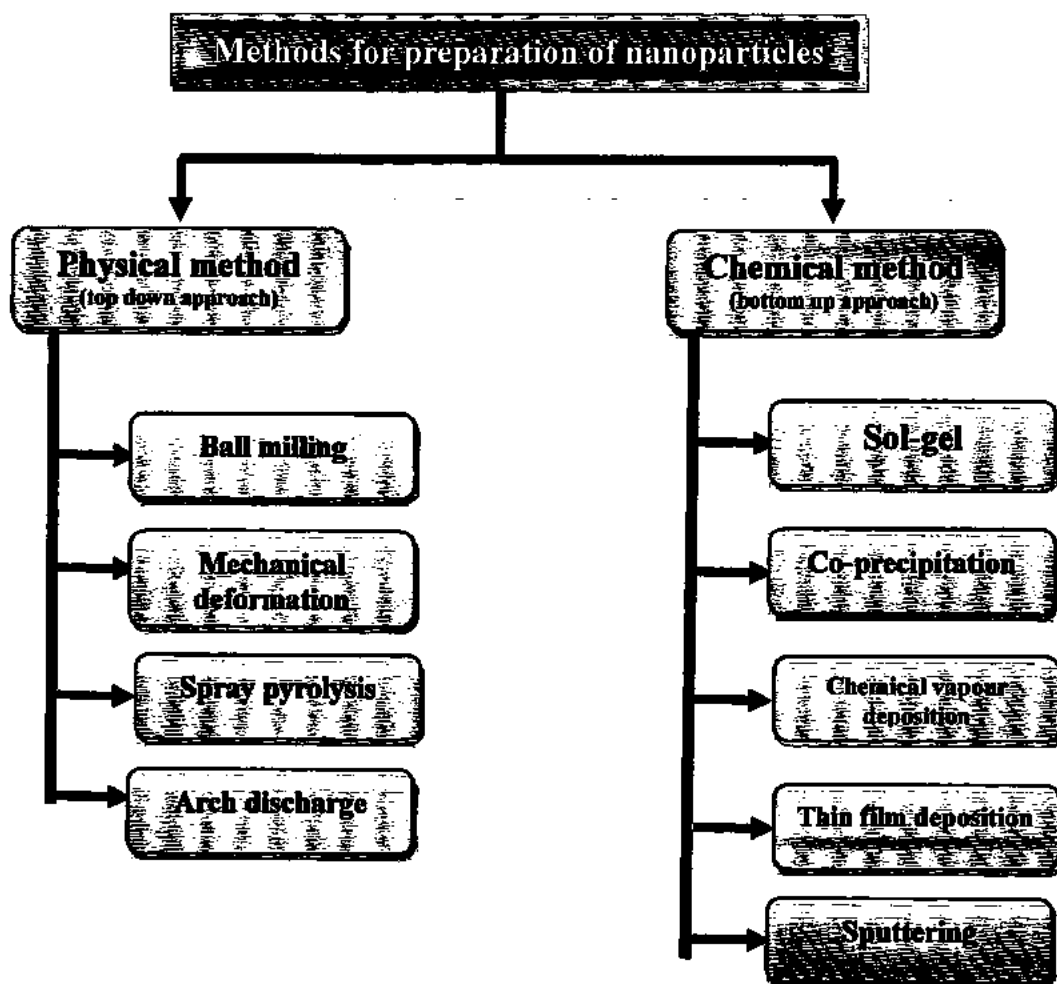
Fig. 0.1: Top-down and bottom-up approaches adopted for nanomaterials.
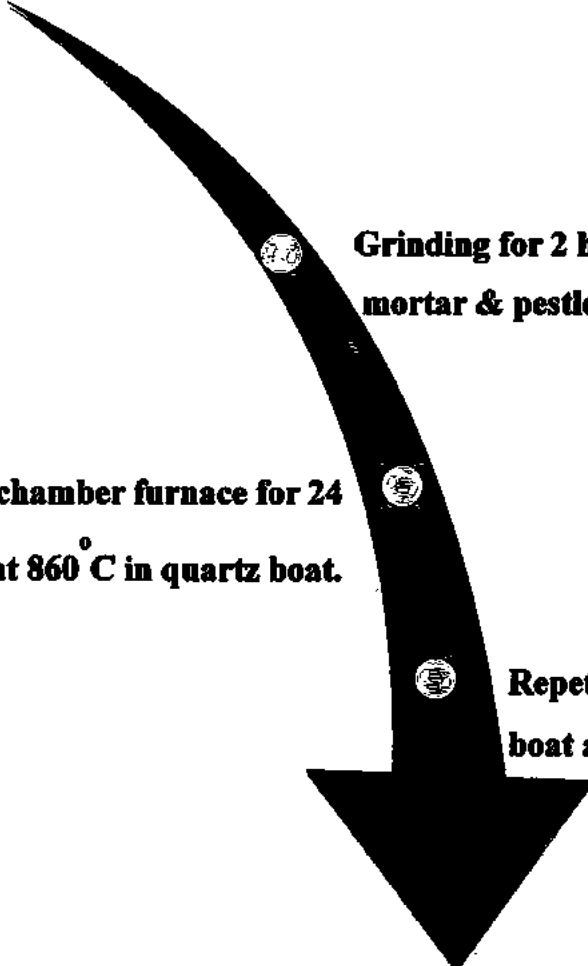
3.2.2 Bottom-up Approach

Chemical method or bottom up approach is extremely significant for the synthesis of nanoparticles. In this technique atoms and molecules are joined together to give the nanoparticles by using different methods. The main advantage of this method is that the particle size will be controlled and the particles with same size and chemical composition can be reproduced. Some of the most commonly used chemical methods are sol-gel, CVD, self-assembly and positional assembly.

3.3 Nanoparticles/superconductor composite

Solid-state reaction method is used to prepare bulk CuTl-1223 superconductor. $Ba(NO_3)_2$, $Ca(NO_3)_2$ and $Cu(CN)$ are used as starting material. The reaction complete in three steps. In first step fixed ratio of $Ba(NO_3)_2$, $Ca(NO_3)_2$ and $Cu(CN)$ were mixed and heated in quartz furnace at 860 °C as shown in Fig. 3.2 . $NiFe_2O_4$ nanoparticles are prepared by using sol-gel method a Fig. 3.3 are then added in appropriate ratios in the precursor material and then it were finely grounded. The mixture is then heated again at 860 °C [6]. In third step, precursor materials were again refined and finally mixed with Tl_2O_3 (99%, Merck) for preparation of $(NiFe_2O_4)_x/Cu_{0.5}Tl_{0.5}Ba_2Ca_2Cu_3O_{10-\delta}$, (x = 0, 0.25% and 0.5%) as composite material as shown in Fig. 3.4. After that the material was pelletized under pressure level of 3.8 tons /cm^3 and then wrapped in a gold capsule in order to reduce Thallium loss during forming at the temperature of 860°C for about 10 min came by blowing out at room temperature [7].

Preparation of $Cu_{0.5}Ba_2Ca_2Cu_3O_{10-\delta}$ precursor

$Cu_2(CN)_2 + Ba(NO_3)_2 + Ca(NO_3)_2$

Grinding for 2 h in agate mortar & pestle.

Firing in chamber furnace for 24 h at 860 ^{o}C in quartz boat.

Repetition of firing process in ceramic boat after intermediate grinding of 1 h.

$Cu_{0.5}Ba_2Ca_2Cu_3O_{10-\delta}$

Fig. 0.2: Preparation of $Cu_{0.5}Ba_2Ca_2Cu_3O_{10-\delta}$ precursor.

Synthesis of NiFe$_2$O$_4$ nanoparticles by Sol-gel method

Iron Nitrate   →   Ethanol   ←   Nickel Nitrate

Citric Acid + Water   Mixed the solutions with constant stirring   Ammonia for PH control

Stirring at 70°C and gel is formed

Dry gel at 110°C in oven for 12 hours

Grind dried gel and annealed at 900°C for 2 h
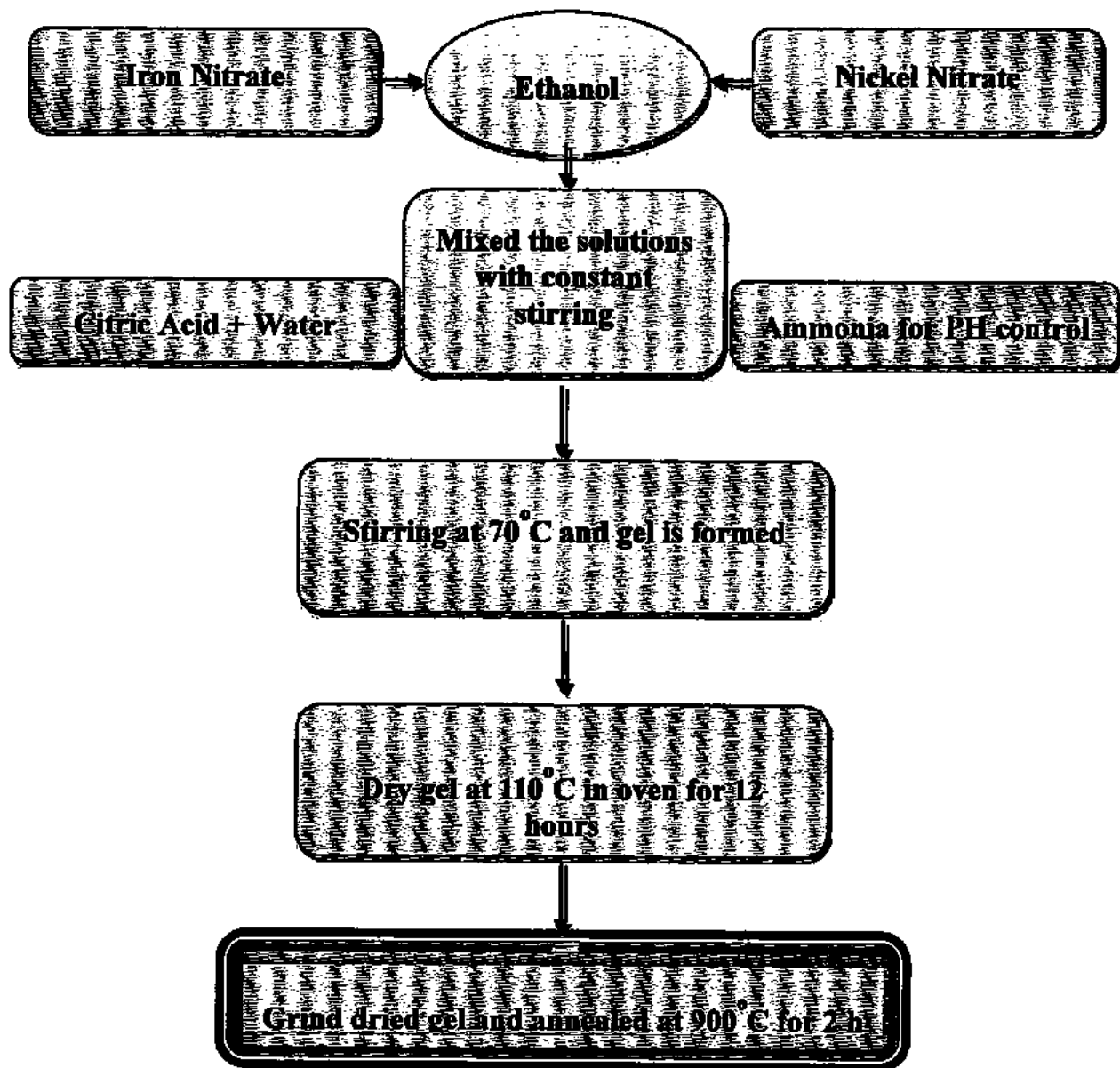
Fig. 0.3: Flow chart for the synthesis of NiFe$_2$O$_4$ nanoparticles by sol-gel method.

$(NiFe_2O_4)_x/CuTl-1223$ nanoparticles-superconductor composites

- $Cu_{0.5}Ba_2Ca_2Cu_3O_{10-\delta}$
- Tl_2O_3
- $NiFe_2O_4$

Mixing in agate mortar and pestle in appropriate ratio

Wrapping in Gold capsule

- Pelletization under $3.8\ tons/cm^2$

- Sintering at $860\ ^0c$ for 10 min in preheated chamber furnace
- Quenching to room temperature

$(NiFe_2O_4)_x/(Cu_{0.5}Tl_{0.5})Ba_2Ca_2Cu_3O_{10-\delta}$
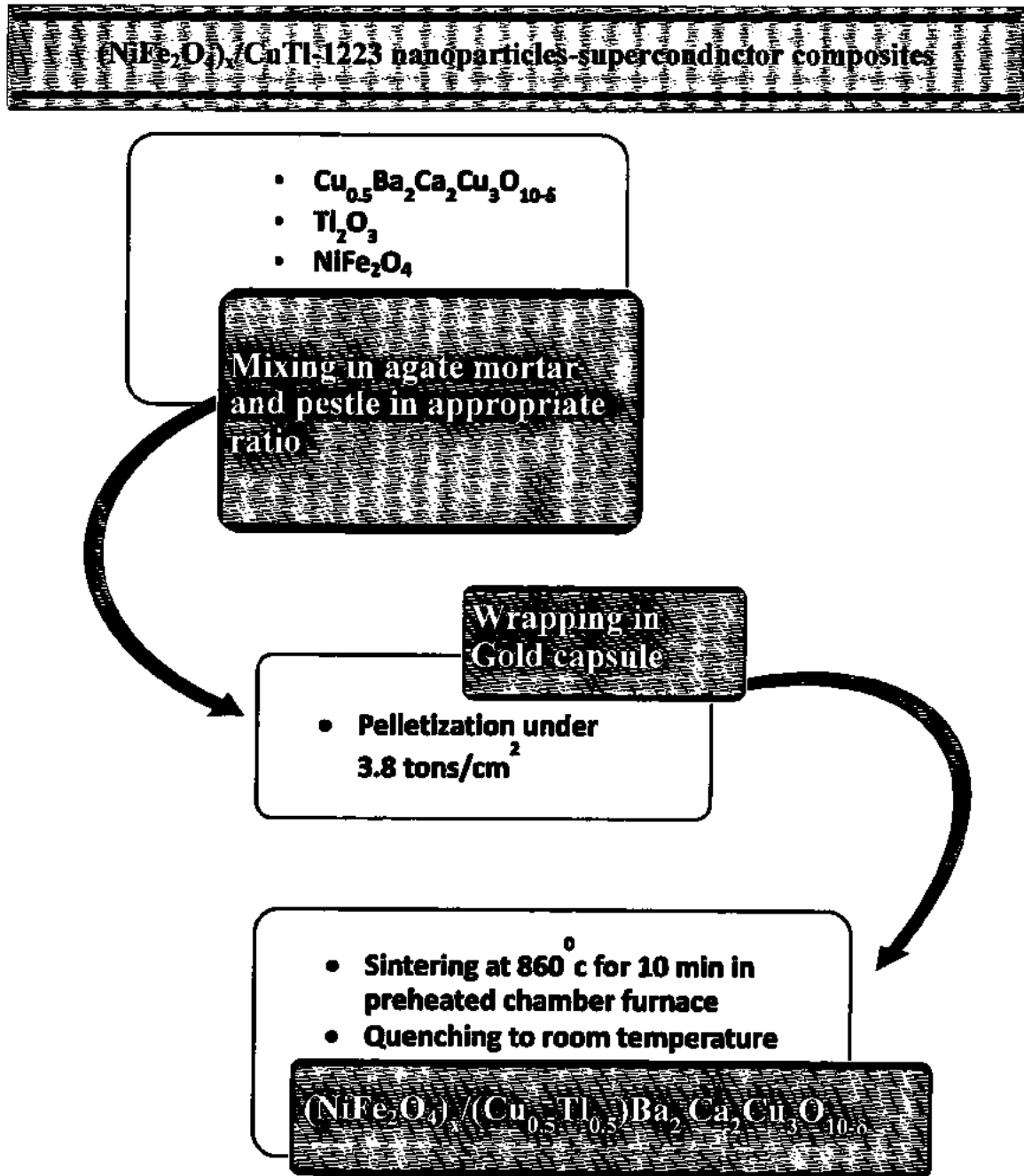
Fig. 0.4: Flow chart to synthesized $(NiFe_2O_4)_x/CuTl-1223$ nanoparticles /superconductor composites.

3.4 Characterization Techniques

Bundle of characterization techniques are used for analysis of nano-structures and nano-composites. Crystal structure was recognized by using X-ray diffraction technique (XRD), infield measurement dc-resistivity versus temperature and other superconducting parameters were measured by using physical properties measuring system (PPMS). Scanning electron microscopy (SEM) is also used to analyze the surface morphology.

3.4.1 X-ray Diffraction (XRD)

X-ray diffraction (XRD) is a useful technique to find out different characteristics of the composites material like crystalline phase, grain sizing of structure, phase composition, imperfections in materials etc. [8]. X-rays are the types of electromagnetic radiations of very small wavelength (0.01-10 nm) their energy is more than the energy of early electromagnetic radiations yielded from interior shell transition. They can penetrate easily into the material because of their very small wavelength [9]. X-rays wavelength is ranging from 0.7 − 2.Å matching to energies of 6 − 17 keV.
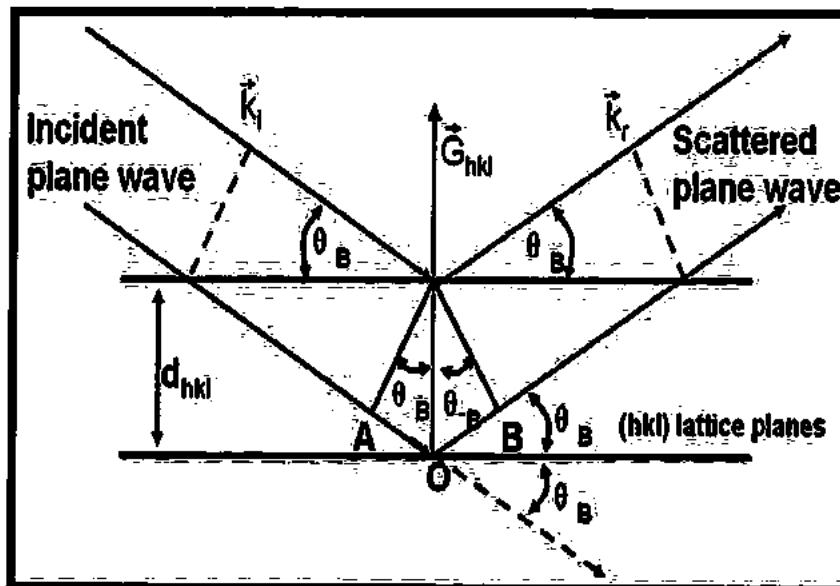
Fig. 0.5: X-ray diffraction pattern from the lattice planes [8].

In this technique, atoms of the crystals made X-rays to diffract at different angles. 3D images for the density of electron can be originated by evaluating the intensity levels and angels of the diffracted beam. From electron density we can take the perspective of electron in the crystal. As it is diffracted through the crystals of interatomic spacing and is reflect from the crystal plane [10]. After the reflection, these rays obey Bragg's Law. i.e,

$$2d(\sin \theta) = n\lambda \dots\dots\dots\dots\dots\dots\dots\dots\dots\dots\dots\dots(3.1)$$

In the above equation n is the positive integer which shows the order of diffraction, d is the inter planner distance while θ is the angle which represents the wave length λ when rays are incident to the plane. When electromagnetic beam interpose constructively, then we get peaks of XRD pattern. XRD pattern from the crystal is shown in fig 3.5. The technique is also used to determine the thickness of the thin films [11]. By using measured intensities the data concerning the atomic placements in multilayer can be extracted.
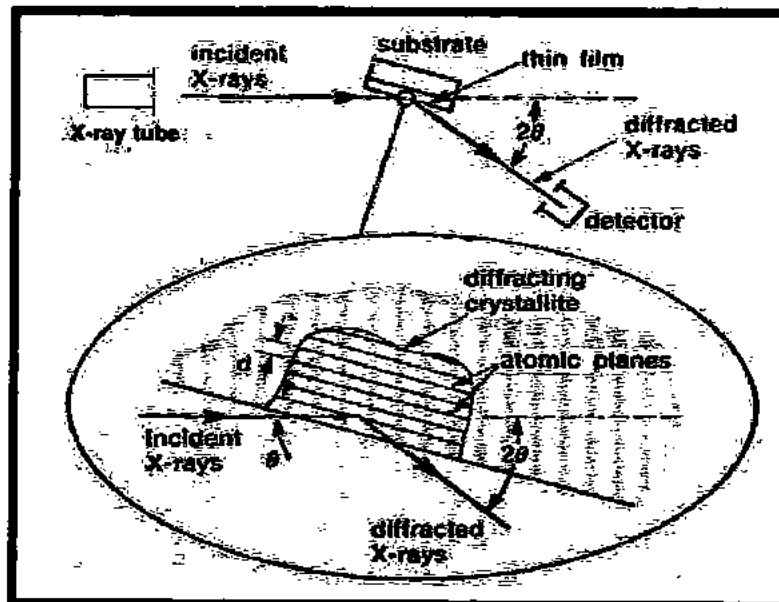
Fig. 0.6: Experimental apparatus of XRD [9].

3.4.2 Scanning Electron Microscope

Scanning electron microscope (SEM) is an encourage structure of microscope that use electronic beam rather than light. High resolution ability provide SEM more useful technique. SEM have a bundle of advantages like broader depth of field. In SEM electromagnets are used rather than lenses for magnification [12].
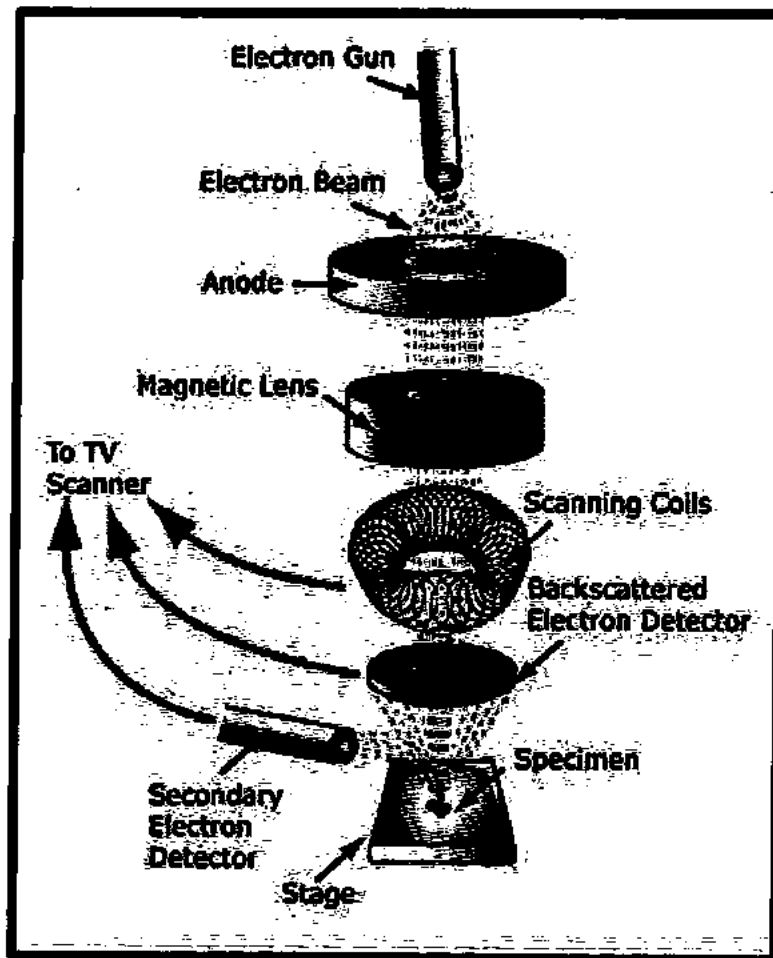
Fig. 0.7: Schematic diagram of SEM [10].

It consists of electron gun through which electrons are ejected, two condenser lenses, objective system and detection system. Electron gun is used to generate and accelerate the electronic

beams with energy 1-30 keV. Three levels of lens demagnetized the   electron beam to focus the beam on sample having diameter of 1-10 nm which containing current 1-100 pA. As the electron probes diameter increases current passing is also increase [13-15]. When the beam of electron is passed off from the electron gun it interacts with the sample. This is responsible for the emission of secondary electrons, back-scattered electron, auger electrons and photons. For the collection of electrons x-rays, sensor are used. At last sensor converts signals into final image.
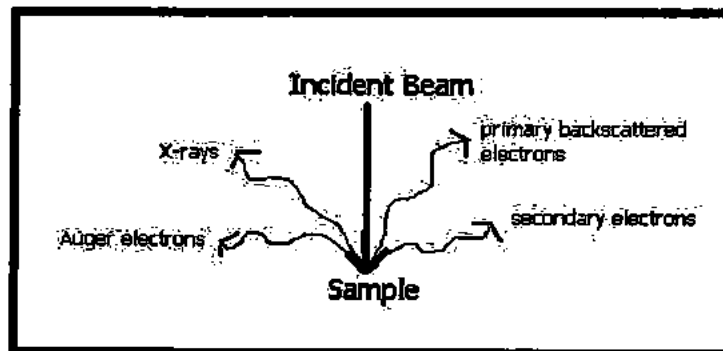
Fig. 0.8: Emission of electrons and photons [15].

3.4.2.1 Secondary Electrons

The electron beam is comes from the electron gun is hits the sample and penetrates into the surface and causing inelastic collision on atoms about the surface of the sample. In this process electrons which are about surface escape from the surface and are called secondary electrons. These are low energy electrons their energy is less than 50 eV. Secondary electrons have the range of 0.5-5 eV [16].

3.4.2.2 Backscattered Electrons

Some of the incidental electrons are scattered back from the more mysterious levels of the samples which make elastic collision and after the numbers of elastic collisions they escape from the sample. These electrons are called back-scattered electrons. The energy rate of these electrons is very high (50 eV) [17].

3.4.2.3 Auger Electrons

Auger electrons are produced as a result of Auger Effect. X-rays are emitted as a result in de-excitation of the atoms towards the ground state. Whenever incident electron releases the electron from first shell to any outer shell as a result hole is generated. This can be filled by electron from outer shell leaving in emission of photon of x-ray spectrum, which is also used to release the electron of higher shell. This released electron is called Auger Electron. These electrons are released from the part close to the surface of the sample. The energy of auger electrons depends upon the structure of the atoms [18].

3.4.3 Physical Property Measurement System (PPMS)

Resistivity measure is very easy technique to give interesting data about the electrical and superconducting properties of the specimen. The measure of electrical resistance and resistivity as a part of temperature gives data nearly to the several temperature dependent electronic phase transitions. This system also gives the data about critical temperature and the quality of specimen. A low resistance is suitable because of the little resistance of the specimen. The measure four-probe technique is used for evaluating resistance of the samples as shown in Fig. 3.9 [19]. To measure the resistivity using this technique, the samples were cut in a rectangular bar shape using a diamond saw. This silver spread is used at the ends of the specimen for current (I) and voltage (V) contacts. Because of low resistance, lean copper wires are linked with silver paint as shown in Fig. 3.9. Plus the entirely gathering was place onto a sample distribution holder, where the wires were associated with leads to the measuring system. This specimen holder is recognized as resistivity puck for evaluating resistivity utilizing a Physical Property Measurement System (PPMS).
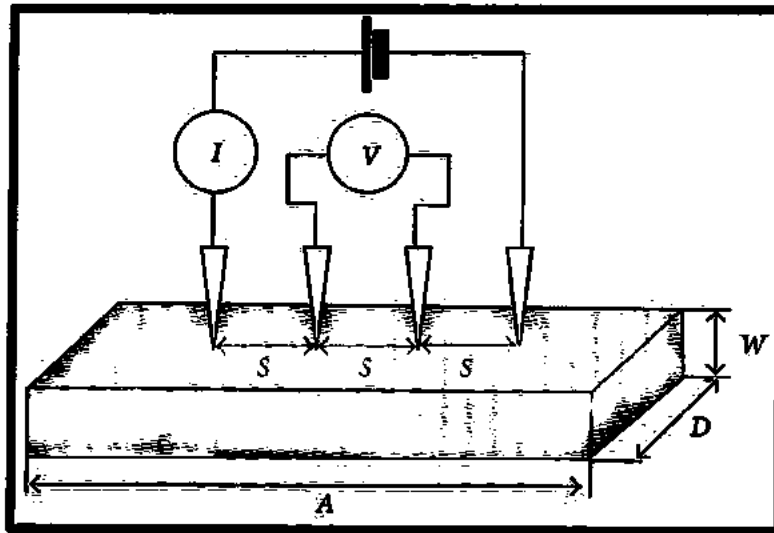
Fig. 0.9: Four probe contacts of current and voltage supplies to the sample during the resistivity measurements [20].

The resistance is estimated utilizing the ohm's law (V = IR), whereas I is the current passed and V is the voltage applied. It is essential to hold the voltage probes among the current probes in a one-dimensional way. The accurate resistivity (ρ) of the sample can be estimated applying the relation,

$$\rho = R\frac{A}{l} \ldots\ldots\ldots\ldots\ldots\ldots\ldots\ldots\ldots\ldots\ldots\ldots\ldots(3.2)$$

Where R is a resistance and A is a cross-sectional area of a specimen. The specimen was cooled by applying liquidized He. The magneto resistive analysis of the specimen, resistance was evaluated by applying the four probe method technique, by applying external magnetic field in a Physical Property Measurement System (PPMS) by Quantum Design as shown in Fig. 3.10. At a fixed applied magnetic field, resistance was measured as an function of temperature from room temperature up to ~ 5 K. Entirely the manganite specimens analyzed in the present work was analyzed by applying this method. PPMS is a versatile and essential instrument used to measure a lot of physical properties e.g d.c/a.c resistivity, specific heat, a.c/d.c magnetizations, thermo-power analysis, halls effect, etc.

Fig. 0.10: PPMS probe and sample chamber geometry [21].
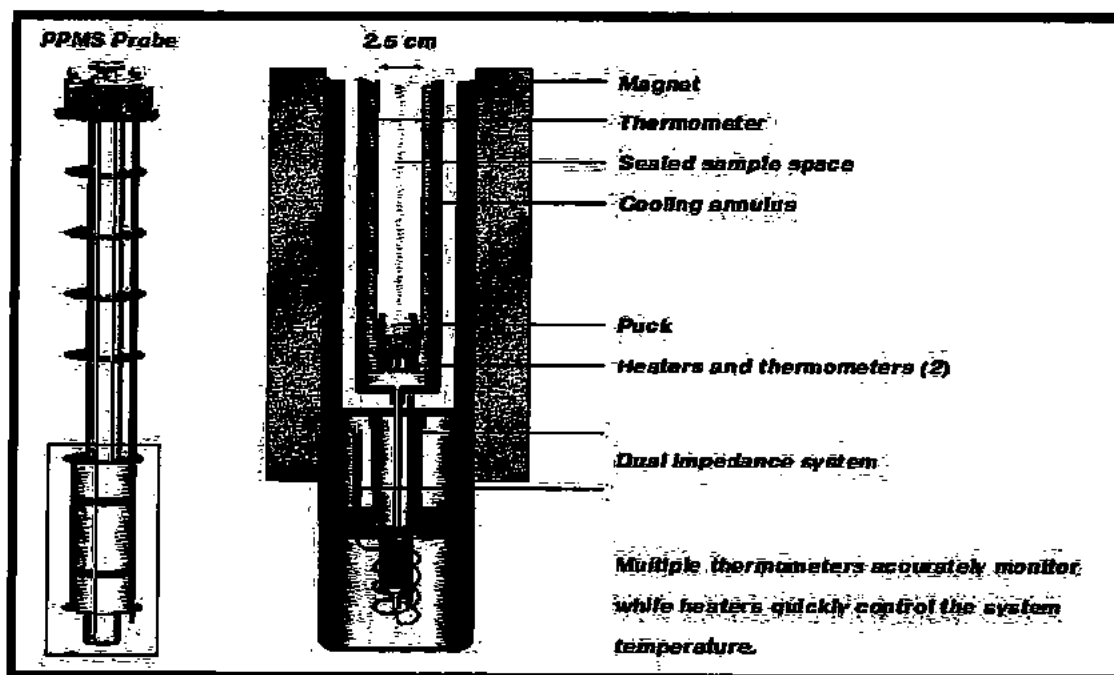
The magneto resistance analyses of bulk specimen, magneto resistance versus temperature of the specimens were expressed by applying the four probe technique in the presence of an external magnetic field using PPMS [22]. The resistivity was evaluated at constant temperature with dissimilar applied field from 1T to 9 T and MR vs. H isotherms having the range of 50-300 K.

References

1. M. Hermann, Thallium-Based High Temperature Superconductors, (Marcel Dekker, Inc. New York USA.41 (1994).

2. C. Torardi, M. A. Subramanian, J. C. Calabrese, J. Gopala krishnan, K. J. Morrissey, T.R.Askew, R.B. Flippen, Chowdhry, and A.W.Sleight Science (Washington, DC, UnitedStates), 240 (4852) (1988).

3. J. Brinker and G. W. Scherer, Sol-Gel Science, Academic Press, Boston, (1990).

4. N. Millot, S. L.Gallet, D. Aymes, F. Bernard and Y. Grin, Journal of the European Ceramic Society 27, 921 (2007).

5. S. Li, L. Liu, V. T. John, C. J. O'Connor, and V. G. Harris, IEEE Transactions on Magnetics. 37, 2350 (2001).

6. M. Srivastava, A. K. Ojha, S. Chaubey, P. K. Sharma and A. C. Pandey, Mater. Sci. Eng. B, 175, 14 (2010).

7. Z. Z. Sheng and A.M. Hermann, Nature 332, 138 (1988).

8. S. S. P. Parkin, V. Y. Lee, E. M. Engler, A. I. Nazzal, T. C. Huang, G. Gorman, R. Savoy, R. Beyers, Phys. Rev. Lett. 60, 2539 (1988).

9. R. Beyers, S.S.P. Parkin, V.Y. Lee, A.I. Nazzal, R. Savoy, G. Gorman, T.C. Huang, S. Laplaca, Appl. Phys. Lett. 53, 432 (1988).

10. S. S. P. Parkin, V.Y. Lee, A. Nazzal, R. Savoy, T.C. Huang, G. Gorman and R. Beyers, Phys. Rev. B 38, 6531 (1988).

11. M. Hervieu, C. Michel, A. Maignan, C. Martin and B. Raveau, Solid State Chem. 74, 428 (1988).

12. M. Hervieu, C. Martin, J. Provost and B. Raveau, J. Solid State Chem. 76, 419 (1988).

13. M. Hervieu, A. Maignan, C. Martin, C. Michel, J. Provost and B. Raveau, J. Solid State Chem, 75, 212 (1988).

14. A. R. West, Solid State Chemistry and Its Applications, John Wiley & Sons (1987).

15. Nawazish A. Khan, Sadaf Aziz, Journal of Alloys and Compounds538, 183–188 (2012).

Synthesis and Experimental Techniques

16. Yoshio Waseda, Eiichiro Matsubara, Kozo Shinoda, X-Ray Diffraction Crystallography, Springer Science & Business Media (2011).

17. B. D Cullity, Elements of x-ray diffraction, 2nd edition, Addison-wesley publishing company, Inc. London (1977).

18. C. Suryanarayana, M. Grant Norton ,X-Ray Diffraction: A Practical Approac,Springer Science & Business Media (1998).

19. M. Dapor, Springer Science, Transport of Energetic Electrons in Solids, Springer (2014).

20. L. Reimer, Scanning Electron Microscopy: Physics of Image Formation and Microanalysis, Springer Science & Business Media (1998).

21. E. Ruckenstein, and S. Narain, Mater. Lett.,**8**, 421 (1989).

22. E. Ruckenstein, and C. T. Cheung, J. Mater. Res. **4**, 1116 (1989).

Chapter no. 4

Results and Discussion

4.1 Crystal structure

X-rays diffraction is used to study the crystal structure of $(NiFe_2O_4)_x/(CuTl-1223)$ nanoparticles-superconductor composites with x = 0, 0.25 and 0.50 wt. %. The X-rays tube was operated at 40 kV and 25mA which employs Cu-Kα rays of wavelength 1.54 nm. Check cell was used for indexing and computing the unit cell parameters. The XRD pattern of $NiFe_2O_4$ nanoparticles is shown in Fig. 4.1. Fig. 4.1 shows that all of the diffraction peaks represents pure $NiFe_2O_4$ spinel ferrite phase. Average crystallite size of the nanoparticles was calculated by using Debye-Scherrer's formula;

$$D = \frac{k\lambda}{\beta cos\theta} \quad\text{..(4.1)}$$

where k is the shape constant and its value is 0.9, λ is the wavelength of X-rays employed, β is the full width at half maxima (FWHM) and θ_B is the diffraction angle. The average crystallite size of the nanoparticles is 35 nm. Fig. 4.2 shows the XRD pattern of $(NiFe_2O_4)_x/(CuTl-1223)$; x=0, 0.25 and 0.5 wt%. composites. Majority of the XRD peaks are indexed well which represents the tetragonal crystal structure of CuTl-1223 phase (P4/mmm space-group) and a very few low intensity un-indexed diffraction peaks indicates the presence of some other superconducting phases as well as some unknown impurities.
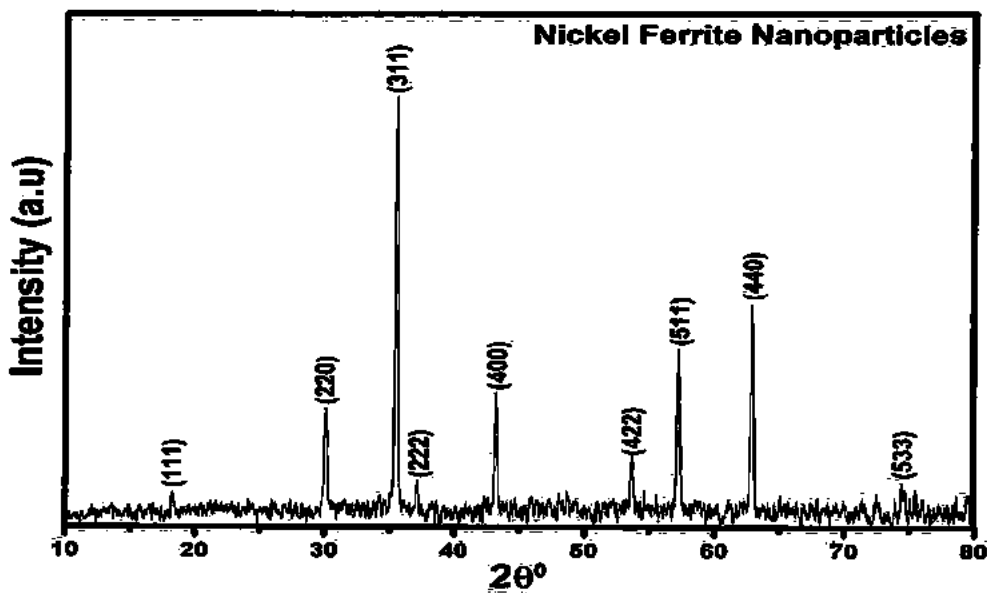
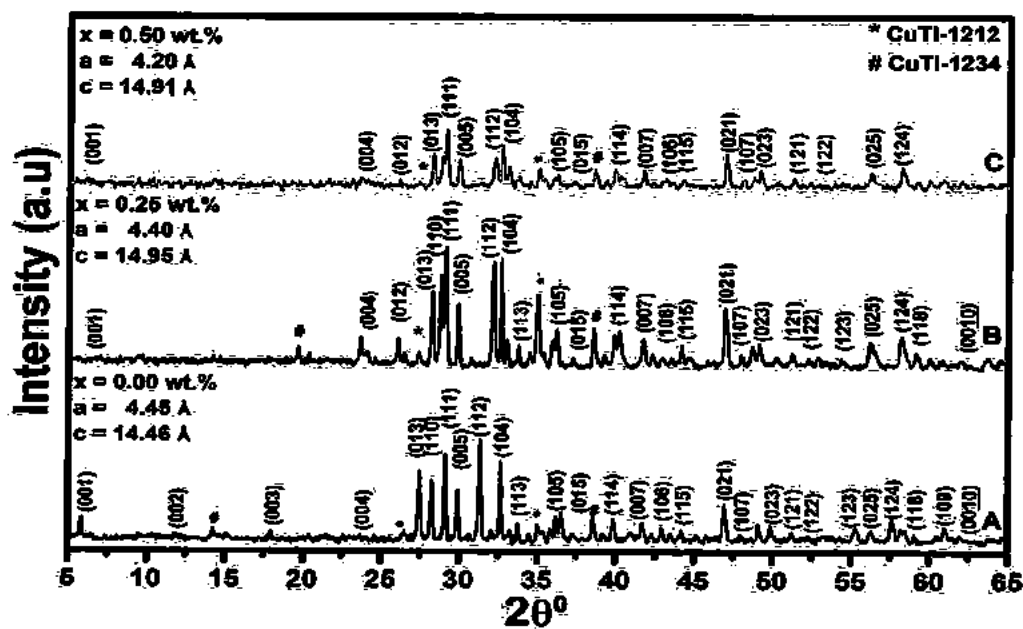Fig. 4.1: XRD pattern of $NiFe_2O_4$ nanoparticles.

Fig. 4.2: XRD patterns of $(NiFe_2O_4)_x$ /(CuTl-1223) superconductor composite samples with (A) x = 0, (B) x = 0.25 (C) x = 0.5 wt. %.

The computed cell parameters of our superconductor composites $(NiFe_2O_4)_x$ /(CuTl-1223) are a= 4.01Å, c = 14.99 Å for x = 0, a = 4.00 Å, c = 14.95 Å for x = 0.25 and a = 3.90 Å, c = 14.91Å for x = 0.5 wt.%, respectively. The addition of $NiFe_2O_4$ nanoparticles does not change the structural symmetry of the bulk CuTl-1223 superconductor which shows that $NiFe_2O_4$ nanoparticles resides at the inter-granular sites. However, a little decrement in the c-axis length occurs due to stresses produced by the addition of nanoparticles and variation of oxygen contents. These studies demonstrate that these nanoparticles does not decompose or substitute any lattice site in the unit-cell of CuTl-1223 but lies at the inter-granular sites i.e. grain boundaries.

4.2 Surface morphology

Scanning electron microscopy (SEM) is used to study the surface morphology of the $(NiFe_2O_4)_x$ /(CuTl-1223) superconductor composites. Fig. 4.3 shows the SEM images of $(NiFe_2O_4)_x$/(CuTl-1223) composite samples in powder form with x = 0.50 wt. % at 5 µm and 1 µm, which shows the typical granular behavior of CuTl-1223 superconductor. The powder was pelletized for the transport measurements and the nanoparticles reside on the compressed grains surfaces.

Fig. 4.3: SEM images of superconductor composite powder with x = 0.50 wt. % at 5 μm and 1 μm scales.

4.3 Resistive transition

Physical property measurement system (PPMS) was used to measure the transport properties of $(NiFe_2O_4)_x/(CuTl-1223)$ superconductor composites samples. The dc-resistivity dependence on temperature of $(NiFe_2O_4)_x/(CuTl-1223)$ superconductor composites samples with x = 0 and 0.5 wt. % under different applied magnetic fields ranging from 0 − 6 T was studied and shown in Fig. 4.4

(a, b, c). As the applied field increases, the $T_{c\,(mf)}$ was not changed much but $T_{c\,(0)}$ shifted towards the low temperature. This decrease in $T_{c\,(0)}$ shows that grain boundaries are involved more in superconductivity than the grains. The $T_{c\,(0)}$ decreases from 103.8 to 79.6 K, 95.36 to 70.99 K and 77.06 to 58.54 K for $(NiFe_2O_4)_x/(CuTl-1223)$; x = 0, 0.25 and 0.50 wt% superconductor composites at applied fields from 0 to 6 T, respectively.
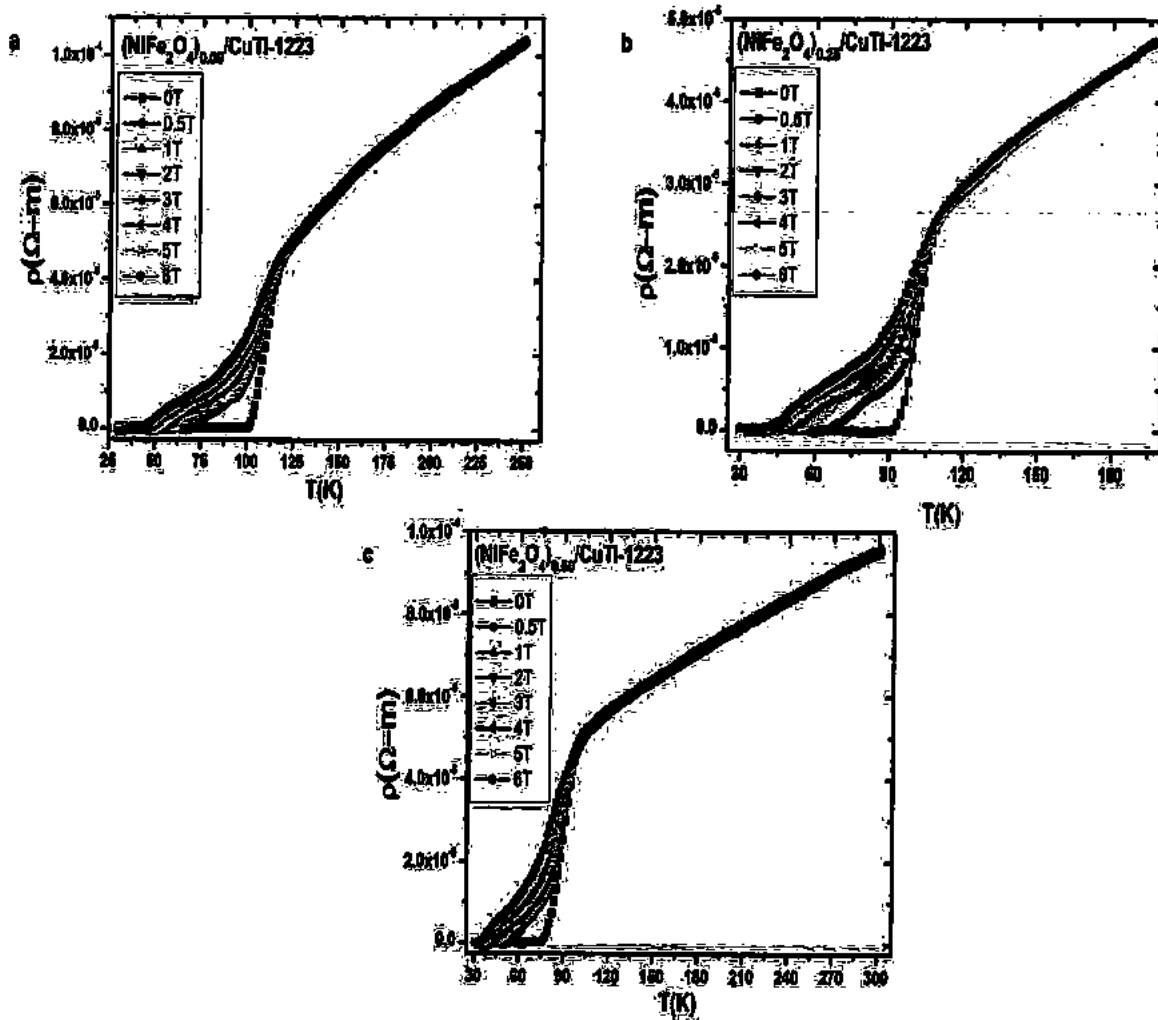

Fig. 4.4: Infield temperature dependence of dc-resistivity of $(NiFe_2O_4)_x/(CuTl-1223)$; (a) x = 0, and (b) x = 0.25 wt.% (c) x = 0.50 wt.% nanoparticles superconductor composites.

$T_{c\,(mf)}$ peaks were observed from the derivatives of infield R-T measurements of $(NiFe_2O_4)_x$/(CuTl-1223) superconductor composites, which may be due to two-step transition in HTSCs. The first step transition occurs at high temperatures when grains become superconducting, and then intra-grain superconductivity starts while the places among grains remain non-superconducting. The second step transition occurred at relatively low temperatures where inter-grains week-link behaves like a Josephson and lock-in phase and get to be superconducting [1-2]. The tailing region in these samples is non-linear due to inhomogeneity and quantum tunneling. It is considered that in the $T_{c\,(0)}$ region of HTSCs is governed by the excitation in the weak-link network. The resistivity broadening was observed in the superconducting states of the composites samples which is due to the thermally activated motion of the vortices. With the increase in applied field, the superconducting transition width was increased, which shows that degree of broadening is sensitive to applied field, this can be analyzed on the basis of thermally activated flux flow (TAFF) model [3]. The superconducting broadening is due to energy dissipation induced by movement of vortices. Hence, this significant resistive broadening in the transition width is the consequence of thermal fluctuations in vortex matter. For all samples, the decrease in $T_{c(0)}$ and $T_{c\,(onset)}$ (K) to the lower value was observed by increasing concentration of $NiFe_2O_4$ nanoparticles and applying external applied field due to TAFF of magnetized vortices.

4.4 Activation Energy

The activation energy $U_o(H, T)$ was determined from the slope of the linear region of low resistivity data which represents the TAFF region in Arrhenius plots as shown in Fig. 4.5 and acts as potential barriers to hold the magnetic-flux in pinning centers. In TAFF, the vortices start hopping from one pinning center to adjacent pinning centers, this gives rise resistance in TAFF region [4-5] and can be written as,

$$\rho(T, H) = \rho_o\,(T, H)\,e^{-U_o/k_B T}\dots\dots\dots\dots\dots\dots\dots\dots\dots\dots\dots\dots(4.2)$$

where k_B is the Boltzmann constant, ρ_o normal state resistivity at temperature just above $T_{c\,(onset)}$ (K), and U_o is the activation energy [6-9]. The Arrhenius plots of the $\ln\rho$ (Ω-m) versus $1/T$ (K^{-1}) for

$(NiFe_2O_4)_x/(CuTl-1223)$ superconductor composites with x = 0, 0.25 and 0.5 wt.% are shown in Fig. 4.5 (a,b,c).
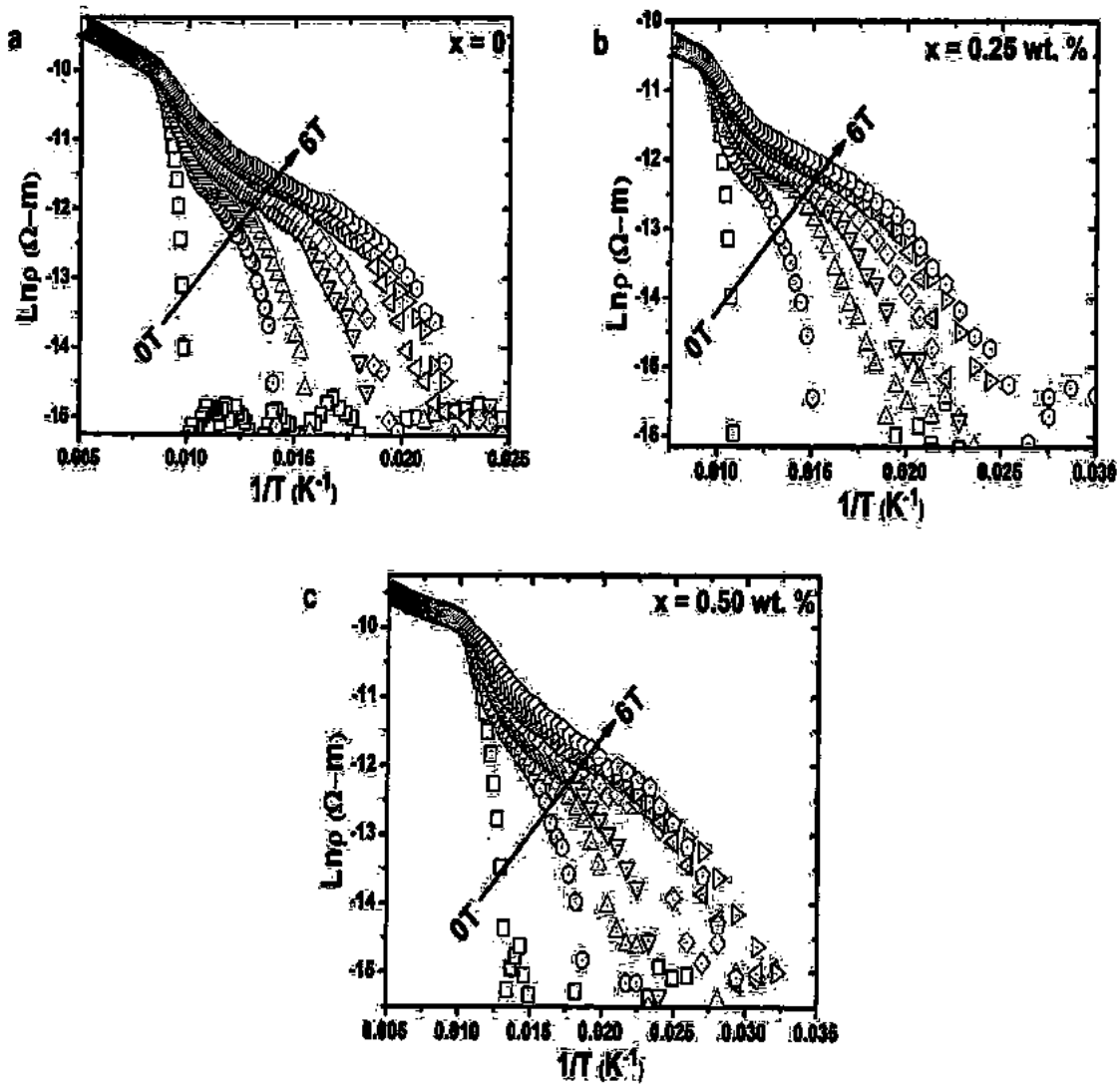

Fig. 4.5: Arrhenius plots of $(NiFe_2O_4)_x/(CuTl-1223)$; (a) x = 0, and (b) x = 0.25 wt.% (c) x = 0.50 wt.% nanoparticles-superconductor composites.

It was observed that activation energy of CuTl-1223 superconductor composite has been decreased with the addition of $NiFe_2O_4$ nanoparticles due to nanoparticles dispersion over the grain-boundaries, which suppressed the inter-grain weak links. The power law dependency of activation energy in magnetic field has already been noticed in different HTSCs families [10-12]. The infield dependency of the U_o for the composites samples is shown in Fig. 4.6, which have been fitted by using power law ($U_o = CH^{-\alpha}$). The measure of α for representative composites with $x = 0$, 0.25 and 0.5 wt.% were found to be 0.76299, 0.56884 and 0.31539, respectively. These measurements express the falling rate of activation energy with the increase in $NiFe_2O_4$ nanoparticles concentration in bulk CuTl-1223 superconductor composite [13]. So the flux pinning ability of the CuTl-1223 superconductor composites have been reduced with the increase of magnetic $NiFe_2O_4$ nanoparticles.

TABLE 4. 1: Field dependent activation energy (U_o)

H (T)	x = 0.00 wt. %	x = 0.25 wt. %	x = 0.50 wt. %
0	0.55431	0.33881	0.19306
0.5	0.26525	0.14611	0.0925
1	0.17113	0.0755	0.05459
2	0.09912	0.04963	0.03161
3	0.07909	0.04391	0.01918
4	0.05606	0.05089	0.02946
5	0.05865	0.04676	0.02511
6	0.04386	0.03818	0.02868

Some important conditions for effective flux pinning are (i) the pinning centers should be nearly equal to the coherence length and (ii) the vortex and the lattice of pinning centers period must correspond with each other [14]. The noticed non-fitted activation energies versus applied magnetic field H(T) is presented in Fig 4.6.
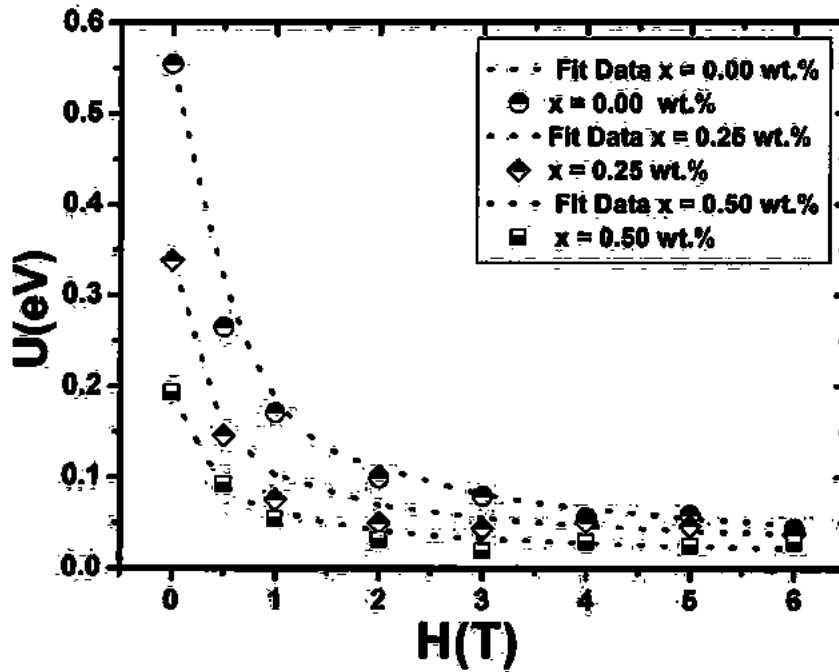
Fig. 4.6: Activation energy (U_o) dependence on magnetic field for $(NiFe_2O_4)_x/(CuTl-1223)$; $x = 0, 0.25$ and 0.50 wt. % nanoparticles-superconductor composite samples. Dotted line shows the theoretical fit of equation $U_o = CH^{-\alpha}$.

Fig. 4.7 shows the transition width $[\Delta T = T_{c(Onset)} - T_{c\ (0)}]$ versus 'H', This plot of 'ΔT' versus 'H' was fitted using TAFF model as shown below in Eq. 4.3.

$$\Delta T = \Delta T_o + CH^n \quad\text{...(4.3)}$$

where ΔT_o is the transition width without magnetic field ($H = 0$), and C is the coefficient which depends upon critical current without magnetic field. The measures of n for $(NiFe_2O_4)_x/(CuTl-1223)$; $x = 0, 0.25$ and 0.5 wt.% superconductor composites were determined to be $0.4614, 0.7740$ and 0.9695, respectively. The value for n is generally $2/3 = 0.66$, which depends upon the type of material [15]. Fig.4.7 shows the increase in ΔT with the addition of $NiFe_2O_4$ nanoparticles concentration in CuTl-1223 superconductors composites, this indicates the decrease in pinning potential.

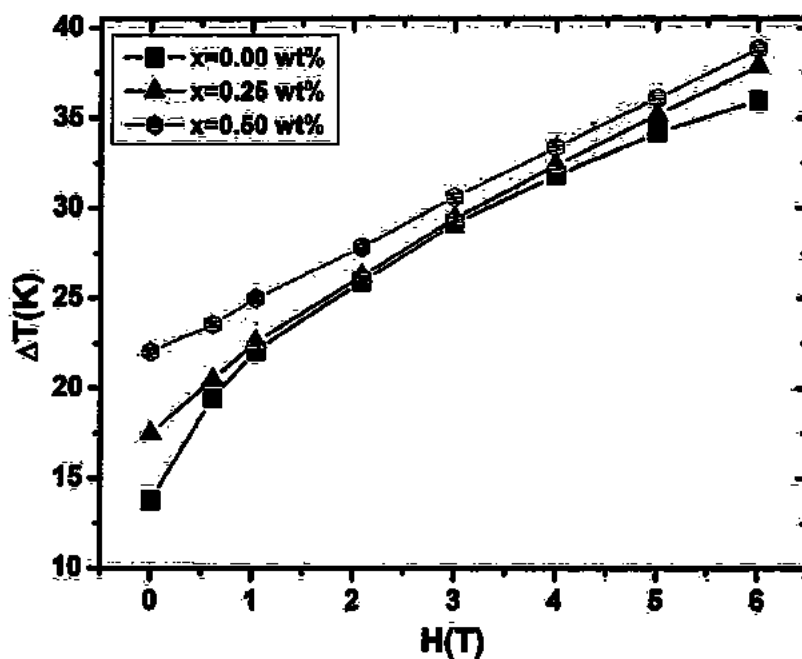**Fig. 4.7:** ΔT verses applied magnetic field H for $(NiFe_2O_4)_x/(CuTl-1223)$; x = 0, 0.25 and 0.50 wt. % nanoparticles-superconductor composites.

A substantial superconducting transition broadening was noticed, which shows the dissipation process and flux creeping in these composite samples. Nearly regular increase in '*ΔT*' indicates that magnetic field lines have been effectively pinned due to which the motion of vortices has been decreased. The superconductor's resistive broadening depends upon applied magnetic field, thermal fluctuation and dissipation phenomenon, which can be computed from the TAFF model.

4.5 Vortex glass Transition

The vortex-phase transition can be understood from the difference in resistive behavior among the vortex-solid and vortex-liquid states. The resistivity broadening in applied field is an evidence of the thermal-fluctuation in the vortex matter [16]. Thus, transport measurements are normally used to analyze vortex-phase transitions. Vortex glass theory is normally used to understand vortex phase

transition in cuprates superconductors. The vortex glass theory suggested for high T_c cuprates [17]. In vortex glass state, at glass-transition temperature T_g, the resistivity diminishes as a power law,

$$\rho = \rho_o \left| \frac{T}{T_g} - 1 \right|^s$$

....(4.4)

Where ρ_o is the normal state characteristic resistivity, s is a constant-quantity which associates the form of disorders. For the glass-line Eq. 4.4, can be re-formulated as [18],

$$\rho = \rho_n \left| \frac{K_B T}{U_o(H,T)} - 1 \right|^s$$

....(4.5)

where U_o is the pinning potential, k_B is the Boltzmann constant and ρ_n is the normal state resistivity. This model shows the occurrence of vortex-solid to vortex-liquid transition depends upon two energy state $U_o(H,T_g) = k_B\,T_g$. This empirical effective pinning energy is expressed as

$$U_o(H,T) = K_B T_c \frac{1-t}{(H/H_o)^\beta}$$

....(4.6)

where $t = T/T_c$, H and β are constants. According to this model, resistance is the result of competition among pinning energy and thermal activation energy $k_B T$. Combining Eqs. (4.5) and (4.6) we get typical resistivity scaling function

$$\rho = \rho_n \left| \frac{T(T_c - T_g)}{T_g(T_c - T)} - 1 \right|^s$$

....(4.7)

From vortex glass model [19] and Eq. (4.7) shows that the resistivity approaches to zero at the T_g as $\rho = c|T - T_g|^s, s = v(1-z)$, where v is the static-exponent relates the glass transition correlation dynamics, $\xi_g \sim (T - T_g)^{-v}$ and z in the dynamic-exponent relates the correlation coefficient time $T_g \sim \xi_g^z$. Thus the Vogel-Fulcher relation $[\partial(\ln \rho)/\partial T]^{-1}$ can be used on resistivity tails to analyze glass transition temperature (T_g) [20-21]. According to this relation, the logarithmic derivative inverse or resistivity linearly dependent on T is given as,

$$\left[\frac{\partial \ln \rho}{\partial T}\right]^{-1} = \frac{1}{s}(T - T_g)$$ ....(4.8)

The temperature dependence of $[\partial(\ln \rho)/\partial T]^{-1}$ under applied fields from $1 - 6$ T for $(NiFe_2O_4)_x/(CuTl-1223)$; x = 0 and x = 0.50 wt.% is shown in Fig. 4.8.

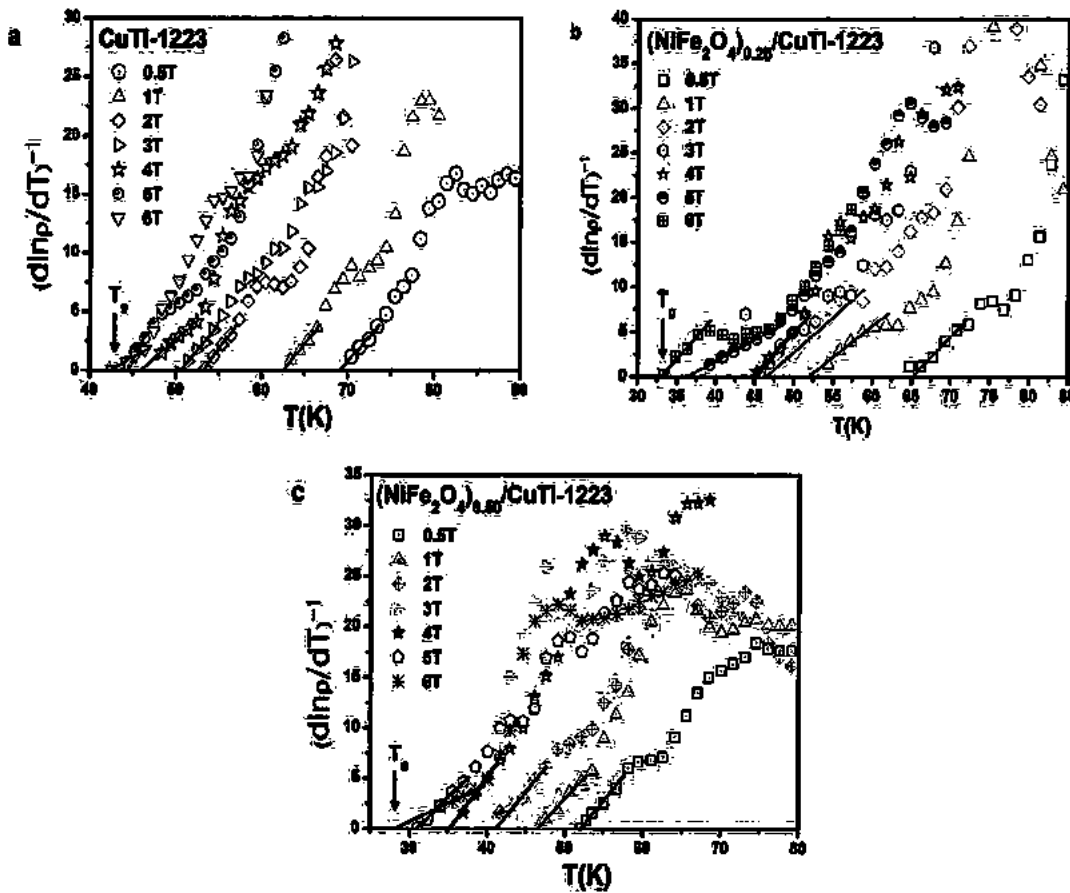**Fig. 4.8:** Determination of the glass transition temperature of $(NiFe_2O_4)_x/(CuTl-1223)$; (a) x = 0 and (b) x = 0.50 wt. % under different applied magnetic fields using Vogel-Fulcher relation.

Through corresponding linear part of the curve from Eq. 4.8, T_g was figured from linear part of low resistivity data. The temperature of upper critical part shows the transition from vortex-glass to vortex-liquid. The values of exponent s and the slope of the fitted straight line are obtained as s = 1/slope for $(NiFe_2O_4)_x/$ (CuTl-1223) ; x = 0, 0.25 and 0.50 wt.%, respectively. For x = 0 wt.%, the s parameter is larger than that obtained for x = 0.25 and 0.5 wt.%. At last combining the observational outcomes over, the obtained vortex phase transition for $(NiFe_2O_4)_x/(CuTl-1223)$; x = 0, 0.25 and

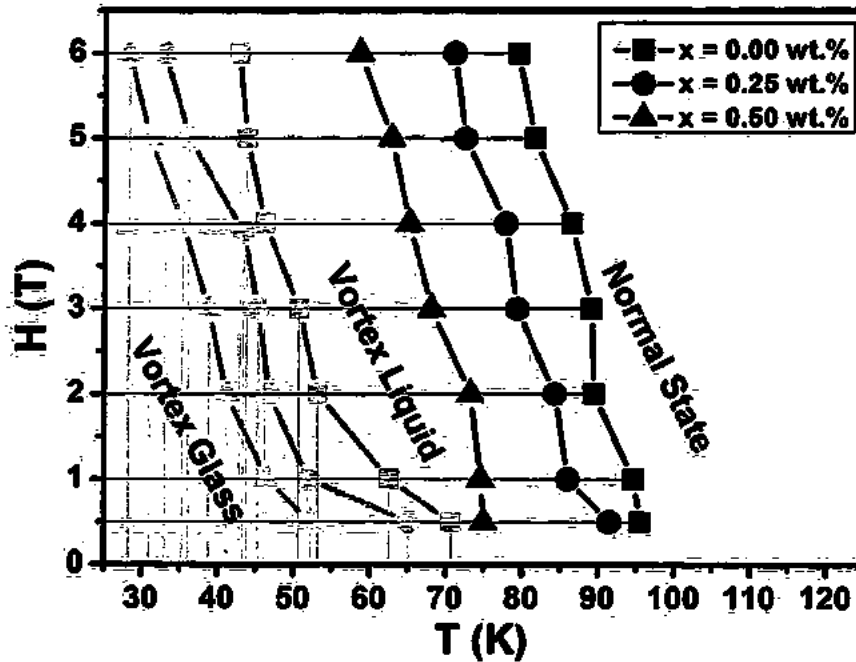0.50 wt.% superconductor composites samples with dissimilar dynamical features are presented in Fig. 4.9.

Fig. 4.9: Vortex phase diagram for the $(NiFe_2O_4)_x/(CuTl-1223)$; x = 0, 0.25 and 0.50 wt. % under different applied magnetic fields.

We developed the vortices phase diagram in the H-T space between T_g and $T_{c(0)}$, associated with vortex-glass to liquid phase-transition. Fig.4.9 shows that T_g and $T_{c(0)}$ changes towards the lower temperature values for x = 0, 0.25 and 0.50 wt.% of $NiFe_2O_4$ nanoparticles added samples. The obtained results confirm that vortex pinning properties have been decreased with the addition of $NiFe_2O_4$ nanoparticles concentration in CuTl-1223 superconducting matrix. According to pinning-model the decrease in T_g and $T_{c(0)}$ is due to disorders caused from thermal fluctuations inside the vortex solid lattice and can be separated into two dissimilar regions according to the strength of the applied magnetic fields [22]. The vortex glass state represents the region below T_g, As applied magnetic fields increases H > H_g, the vortex glass turns softer and finally melts and converted into vortex liquid, which holds middle region between T_g and $T_{c(0)}$, where thermal fluctuations are

important in the vortex phases which are responsible for dimensionality transition from 2D to 3D and above $T_{c\ (0)}$ the sample move towards normal state [23-25]. The $NiFe_2O_4$ nanoparticles added superconductor composites with different concentrations x = 0, 0.25 and 0.50 wt.% shows very narrow regions of vortex-glass phase, which shows weak pinning behavior at T_g.

Conclusions

We have synthesized the composites of $NiFe_2O_4$ nanoparticles added CuTl-1223 superconductor composites successfully. We have investigated the effect of $NiFe_2O_4$ nanoparticles addition on structural, morphological and infield response of CuTl-1223 superconducting matrix. The crystal structural symmetry of CuTl-1223 superconductor was not varied by the addition of $NiFe_2O_4$ nanoparticles. The temperature dependent infield dc-resistivity has been explained by thermally activated flux flow (TAFF) model. Some parameters like glass transition temperature T_g, magnetic field dependent activation energy $U_o\ (H)$ and transition width ΔT calculated from TAFF model were decreased with the increase in applied magnetic field. That shows the diffusion of nanoparticles across the grain-boundaries of bulk CuTl-1223 superconducting matrix. The double transitions for all concentrations of $NiFe_2O_4$ indicate the existence of vortex-glass phase.

References

1. J. Ding, X. Xiang, Y. Zhang, H. Liu, and X. Li, Phys. Rev. B **77**, 214524 (2008).

2. G.Yildirim, S. Bal, and A.Varilci, J. Supercond. Nov. Magn. **25**, 1665 (2012).

3. G. Yildirim, M. Dogruer, O. Ozturk, A. Varilci, C. Terzioglu, and Y. Zalaoglu, J. Supercond. Nov. Magn. **25**, 893 (2012).

4. Y. Wang and H.-H. Wen, Euro phys. Lett. **81**, 57007 (2008).

5. M. Nikolo, X. Shi, J. Jiang, J.Weiss, and E. Hellstrom, J. Supercond. Nov. Magn. **27**, 1983 (2014).

6. Maiorov, Katase, S. A. Baily, H. Hiramatsu, T. G. Holesinger, H. Hosono, Supercond. Sci. Technol. **24**, 055007, (2011).

7. C. Tarantini, S. Lee, Y. Zhang, J. Jiang, C.W. Bark, J. D. Weiss, Appl. Phys. Lett. **96** 142510, (2010).

8. M. Waqee-ur-Rehman, I. Qasim, M. Mumtaz, K. Nadeem, and A. Khurram, Physica B **476**, 37 (2015).

9. H. Lei, R. Hu, E. Choi, C. Petrovic, Phys. Rev. B, **82**, 134525 (2010).

10. Mellekh, M. Zouaoui, F. Ben Azzouz, M. Annabi, M. Ben Salem, Solid State Communications. **140**, 318 (2006).

11. C. Shekhar, A. Srivastava, P. Kumar, P. Srivastava, O.N. Srivastava, Supercond. Sci. Technol. **25**, 045004, (2012).

12. Y. Yeshurun, A .P. Malozemoff, Phys. Rev. Lett. **60**, 2202, (1988).

13. M. Shahbazi, X. L. Wang, Z. W. Lin, J. G. Zhu, J. Appl. Phys. **109**, 07151, (2011).

14. D. L. Sun, Y. Liu, C. T. Lin , Phys. Rev. B, **80**, 144515, (2009).

15. V.V. Schmidt, The Physics of Superconductors: Springer-Verlag, Berlin Heidelberg, Germany, 126–132 (1997).

16. J. Jaroszynski, F. Hunte, L. Balicas, Youn-jung Jo, I. Raičević, A. Gurevich, Phys. Rev. B **78** 174523, (2008).

17. A. K, Pramanik, L. Harnagea, S. Singh, S. Aswartham, G. Behr, S. Wurmeh, C. Hess, Phys. Rev. B, **82** 014503, (2010).

18. Y. J. Song, B. Kang, J. S. Rhee, Y. Kwon, Europhys. Lett. **97** 47003, (2012)

19. Fisher D. S., Fisher M. P. A, Huse D. A, Phys. Rev. B, **43**, 130, (1991)

20. H. J. Kim, W. N. Kang, E. I. Choi, M. S. Kim, K. H. P. Kim, S. I. Lee, Phys. Rev. Lett. **87**, 087002 (2001).

21. D. S. Fisher, D. A. Huse, Phys. Rev. B **43**, 1 (1991).

22. T. Palstra, A. Batlogg, R. Van Dover, L. Schneemeyer, J. Waszczak, Phys. Rev. B **41**, 6621 (1990).

23. Andersson M, Rydh A, O. Rapp, Phys. Rev. B **63**, 184511, (2001)

24. Fisher M. P. A. Phys. Rev. Lett. **62**, 1415, (1989)

25. P. W. Anderson, Phys. Rev. Lett. **9**, 309 (1962)